Vol. 30, No. 11, November 2006   ISSN 0955-7997

ENGINEERING ANALYSIS *with* BOUNDARY ELEMENTS

Special Issue

ENGINEERING
ANALYSIS *with*
BOUNDARY
ELEMENTS

Null-field approach for piezoelectricity problems with arbitrary circular inclusions

Jeng-Tzong Chen*, An-Chien Wu

Department of Harbor and River Engineering, National Taiwan Ocean University, Keelung 20224, Taiwan

Abstract

In this paper, we derive the null-field integral equation for piezoelectricity problems with arbitrary piezoelectric circular inclusions under remote anti-plane shears and in-plane electric fields. Separable expressions of fundamental solutions and Fourier series for boundary densities are adopted to solve the piezoelectric problem with circular inclusions. Four gains are obtained: (1) well-posed model, (2) singularity free, (3) boundary-layer effect free and (4) exponential convergence. The solution is formulated in a manner of semi-analytical form since error purely attributes to the truncation of Fourier series. Two piezoelectric problems with two piezoelectric circular inclusions are revisited and compared with the Chao and Chang's solutions to demonstrate the validity of our method. The limiting case that the two inclusions separate far away leads to the Pak's solution of a single inclusion. Stress and electric field concentrations are calculated and are dependent on the distance between the two inclusions, the mismatch in the material constants and the magnitude of mechanical and electromechanical loadings. The results for the shear and electric loadings in two directions are also compared well with the Wang and Shen's results.
© 2006 Elsevier Ltd. All rights reserved.

1. Introduction

The distribution of stress in an infinite medium containing circular holes and/or inclusions under the remote anti-plane shear has been studied by many investigators. However, analytical solutions are rather limited except for simple cases. To the authors' best knowledge, an exact solution of a single inclusion was derived by Honein et al. [1] using the complex potential. Besides, analytical solutions for two identical holes and inclusions were obtained by Stief [2] and by Budiansky and Carrier [3], respectively. Zimmerman [4] employed the Schwartz alternative method for plane problems with two holes or inclusions to obtain a closed-form approximate solution. In addition, Sendeckyj [5] proposed an iterative scheme for solving problems of multiple inclusions. However, the approach is rather complicated and explicit solutions were not provided.

Numerical solutions for problems with two unequal holes and/or inclusions were provided by Honein et al. [1] using the Möbius transformations involving the complex potential. Not only anti-plane shears but also screw dislocations were considered. Numerical results were presented by Goree and Wilson [6] for an infinite medium containing two inclusions under the remote shear. Bird and Steele [7] used a Fourier series procedure to revisit the anti-plane elasticity problems of Honein et al.'s paper [1]. To approximate the infinite problem, an equivalent bounded-domain approach with stress applied on the outer boundary was utilized. A shear stress σ_{zr} on the outer boundary is used in place of a stress σ_{zy} at infinity to approach the Honein et al.'s results as the radius becomes large. Based on the technique of analytical continuity and the method of successive approximation, Chao and Young [8] studied the stress concentration on a hole surrounded by two inclusions. For a triangle pattern of three inclusions, Gong [9] employed the complex potential and Laurent series expansion to calculate the stress concentration. Complex variable boundary element method (CVBEM)

*Corresponding author. Tel.: +886 2 24622192x6177;
fax: +886 2 24632375.

E-mail address: jtchen@mail.ntou.edu.tw (J.-T. Chen).

was utilized to deal with the problem of two circular holes by Ang and Kang [10] and Chou [11], independently.

Mathematically speaking, only circular boundaries in an infinite domain are concerned here. Mogilevskaya and Crouch [12] have also employed Fourier series expansion technique and used the Galerkin method instead of collocation technique to solve the problem of circular inclusions in 2-D elasticity. Also Wang et al. [13] proposed a fast algorithm for large-scale problems. The advantage of their method is that one can tackle a lot of inclusions even inclusions touching one another. However, they did not expand the fundamental solution into the degenerate kernels in the polar coordinate. Degenerate kernels play an important role not only for mathematical analysis [14], but also for numerical implementation [15]. For example, the spurious eigenvalue [16], fictitious frequency [17] and degenerate scale [18] have been mathematically and numerically studied by using degenerate kernels for problems with circular boundaries. One gain is that exponential convergence instead of algebraic convergence in boundary element method (BEM) can be achieved using the degenerate kernel and Fourier expansion [15]. Chen et al. [19] have successfully solved the anti-plane problem with circular holes using the null-field integral equation in conjunction with degenerate kernels and Fourier series. The idea was also applied to determine torsional rigidities of circular bars with circular holes [20]. The extension to biharmonic problems was also implemented [21]. The above literature review focuses on the elasticity problems with circular holes and/or inclusions. We will extend to piezoelectricity problems.

The recent technological developments and the increasing market demand have opened promising research opportunities and engineering priorities in the field of micromechanics. Coupled electro-elastic analysis in smart composites and micro-electro-mechanical systems (MEMS) receives much attention. Due to the intrinsic coupling effect of electrical and mechanical fields, the piezoelectric material is widely applied to intelligent structures. Regarding the piezoelectric circular inclusions, an exact solution of a single piezoelectric inclusion was derived by Pak [22] under remote anti-plane shear and in-plane electric loadings. For the two piezoelectric inclusions, Honein et al. [23] employed the Möbius transformation to derive the electromechanical field. Based on the method of analytical continuation and the techniques of successive approximation, Chao and Chang [24] revisited the problem of two piezoelectric inclusions. Wu and Funami [25] also solved this problem by using the conformal mapping and the theorem of analytical continuation. Wang and Shen [26] considered the shear and electric loadings in two directions.

This paper extends the null-field formulation to solve piezoelectricity problems with multiple piezoelectric circular inclusions. By introducing a multi-domain approach, an inclusion problem can be decomposed into two parts. One is the infinite medium with circular holes and the other is the problem with each circular inclusion. After considering

the continuity and equilibrium conditions on the interface for electrical and mechanical fields, a linear algebraic system can be obtained and the unknown Fourier coefficients in the algebraic system can be determined. Then the displacement field and electric potential are obtained. Furthermore, an arbitrary number of circular inclusions are treated by using the present method without any difficulty. The calculation of potential gradient must be determined with care by using the vector decomposition and the adaptive observer system for the nonconfocal case. Also the boundary stress and electric fields can be easily determined by using series sums instead of employing the sense of Hadamard principal value. A general purpose program for arbitrary number of piezoelectric circular inclusions with various radii and different positions was developed. Several examples solved previously by other researchers [22,24,26] were revisited to see the accuracy and efficiency of the present formulation. The Pak's solution of a single inclusion is designed as a limiting case when two inclusions dispart far away.

2. Problem statement of anti-plane displacement field and in-plane electric potential

The physical problem to be considered is shown in Fig. 1, where multiple piezoelectric circular inclusions are imbedded in an infinite piezoelectric medium under the far-field anti-plane shear σ_{zx}^∞, σ_{zy}^∞ and the far-field in-plane electric field E_x^∞, E_y^∞. Bleustein [27] has found that if one takes the plane normal to the poling direction as the plane of interest, only the anti-plane displacement w couples with the in-plane electric field E_r and E_θ. Therefore, we only consider the anti-plane displacement and the in-plane electric field such that

$$u = v = 0, \quad w = w(r,\theta), \quad E_r = E_r(r,\theta),$$
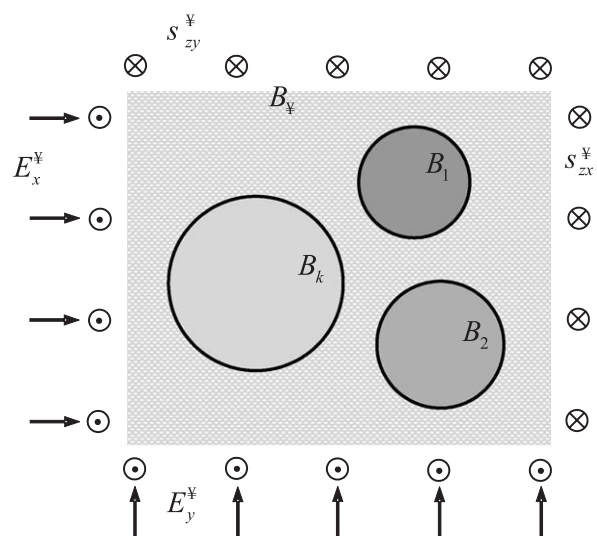$$E_\theta = E_\theta(r,\theta), \quad E_z = 0, \tag{1}$$

Fig. 1. Infinite anti-plane piezoelectric problem with arbitrary piezoelectric circular inclusions under remote shear and electric loadings.

where u, v and E_z are the vanishing components of displacements and electric field, respectively. The governing equation, in the absence of body forces and body charges, can be decoupled and simplified to

$$\nabla^2 w = 0, \quad \nabla^2 \Phi = 0, \tag{2}$$

where ∇^2 is the 2-D Laplacian operator

$$\nabla^2 \equiv \frac{\partial^2}{\partial r^2} + \frac{1}{r}\frac{\partial}{\partial r} + \frac{1}{r^2}\frac{\partial^2}{\partial \theta^2}, \tag{3}$$

and Φ is the in-plane electric potential. The coupling between the elastic field and the electrical field occurs only through the constitutive equations

$$\sigma_{zr} = c_{44}\gamma_{zr} - e_{15}E_r, \quad \sigma_{z\theta} = c_{44}\gamma_{z\theta} - e_{15}E_\theta, \tag{4}$$

$$D_r = e_{15}\gamma_{zr} + \varepsilon_{11}E_r, \quad D_\theta = e_{15}\gamma_{z\theta} + \varepsilon_{11}E_\theta, \tag{5}$$

where c_{44} is the elastic modulus, e_{15} is the piezoelectric constant, ε_{11} is the dielectric constant, σ_{ij} and D_i are, respectively, the anti-plane shear stress and in-plane electric displacement, γ_{ij} and E_i are, respectively, the anti-plane shear strain and in-plane electric field, which are defined as

$$\gamma_{zr} = \frac{\partial w}{\partial r}, \quad \gamma_{z\theta} = \frac{1}{r}\frac{\partial w}{\partial \theta}, \quad E_r = -\frac{\partial \Phi}{\partial r},$$

$$E_\theta = -\frac{1}{r}\frac{\partial \Phi}{\partial \theta}. \tag{6}$$

The analogy between the anti-plane shear deformation and in-plane electrostatics for anti-plane piezoelectric problems is listed in Table 1. By taking free body along the interface between the matrix and inclusions, the problem can be decomposed into two systems. One is an infinite medium with N circular holes under remote anti-plane shear and in-plane electric loadings as shown in Fig. 2(a). The other is N circular inclusions bounded by the B_k contour which satisfies the Laplace equation as shown in Fig. 2(b). From the numerical point of view, this is the so-called multi-domain approach. For the problem in Fig. 2(a), it can be superimposed by two parts. One is an infinite medium under remote shear and electric loadings and the other is an infinite medium with N circular holes which satisfies the Laplace equation as shown in Figs. 2(c)

and (d), respectively. Therefore, one exterior problem for the matrix is shown in Fig. 2(d) and several interior problems for nonoverlapping inclusions are shown in Fig. 2(b). The two problems in Figs. 2(d) and (b) can be solved in a unified manner since they both satisfy the Laplace equation.

When the coupled effect between the mechanical and electrical fields is absent or the piezoelectric constant is equal to zero, the expressions of the electro-elastic field in the present formulation reduces to the results given by Emets and Onofrichuk [28] and Honein et al. [1], respectively.

3. A unified formulation for exterior and interior Laplace problems under anti-plane mechanical and in-plane electrical loadings

3.1. Dual boundary integral equations and dual null-field integral equations

The boundary integral equation (BIE) for the domain point can be derived from the third Green's identity [29], we have

$$2\pi w(x) = \int_B T(s,x)w(s)\,\mathrm{d}B(s) - \int_B U(s,x)t(s)\,\mathrm{d}B(s), \quad x \in D, \tag{7}$$

$$2\pi \frac{\partial w(x)}{\partial \mathrm{n}_x} = \int_B M(s,x)w(s)\,\mathrm{d}B(s) - \int_B L(s,x)t(s)\,\mathrm{d}B(s), \quad x \in D, \tag{8}$$

where $w(x)$ is the anti-plane displacement field, $t(s) = \partial w(s)/\partial \mathrm{n}_s$, s and x are the source and field points, respectively, B is the boundary, D is the domain of interest, n_s and n_x denote the outward normal vector at the source point s and field point x, respectively, and the kernel function $U(s,x) = \ln r$, $(r \equiv |x-s|)$, is the fundamental solution which satisfies

$$\nabla^2 U(s,x) = 2\pi\delta(x-s) \tag{9}$$

Table 1
Analogy between the anti-plane shear deformation and in-plane electrostatics for anti-plane piezoelectric problems

Anti-plane shear deformation	Constitutive equations for anti-plane piezoelectricity	In-plane electrostatics
z-displacement w		Electric potential Φ
Strain γ_{zi}		Electric field E_i
Stress σ_{zi}		Electric displacement D_i
Shear modulus μ		Dielectric constant ε
Body force f		Charge density ρ^*
Strain-displacement relationship $\gamma_{zi} = w_{,i}$	Coupling effect	Electricity $E_i = -\Phi_{,i}$
Constitutive law $\sigma_{zi} = \mu\gamma_{zi}$	$\sigma_{zi} = c_{44}\gamma_{zi} - e_{15}E_i$ $D_i = e_{15}\gamma_{zi} + \varepsilon_{11}E_i$	Constitutive law $D_i = \varepsilon E_i$
Governing equation of equilibrium $\sigma_{zi,i} = -f_z$		Governing equation of Maxwell $D_{i,i} = \rho$
Poisson equation $\nabla^2 w = -f/\mu$		Poisson equation $\nabla^2\Phi = -\rho/\varepsilon$

*Here, ρ is the charge density. The subscript "," refers to partial differentiation with respect to the subsequent spatial coordinate "i".
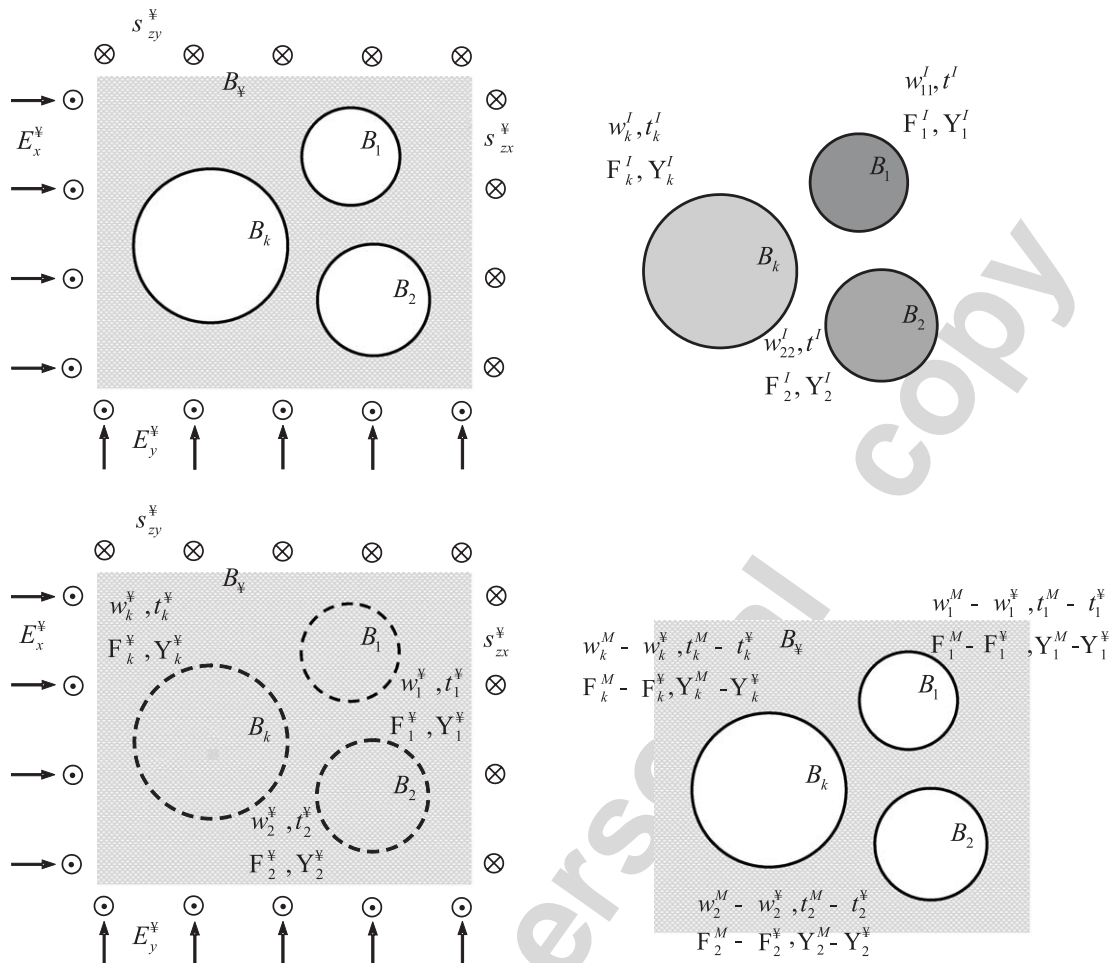
Fig. 2. (a) Infinite piezoelectric medium with circular holes under remote shear and electric loadings. (b) Interior Laplace problems for each piezoelectric inclusion. (c) Infinite piezoelectric medium under remote shear and electric loadings. (d) Exterior Laplace problems for the piezoelectric medium.

in which $\delta(x-s)$ denotes the Dirac-delta function. The other kernel functions, $T(s,x)$, $L(s,x)$ and $M(s,x)$, are defined by

$$T(s,x) \equiv \frac{\partial U(s,x)}{\partial n_s}, \quad L(s,x) \equiv \frac{\partial U(s,x)}{\partial n_x},$$

$$M(s,x) \equiv \frac{\partial^2 U(s,x)}{\partial n_s \partial n_x}. \tag{10}$$

By collocating x outside the domain ($x \in D^c$), we obtain the dual null-field integral equations as shown below

$$0 = \int_B T(s,x)w(s)\,dB(s) - \int_B U(s,x)t(s)\,dB(s), \quad x \in D^c, \tag{11}$$

$$0 = \int_B M(s,x)w(s)\,dB(s) - \int_B L(s,x)t(s)\,dB(s), \quad x \in D^c, \tag{12}$$

where D^c is the complementary domain. Based on the separable property, the kernel function $U(s,x)$ is expanded into the degenerate form by separating the source point

and field point in the polar coordinate [30]:

$$U(s,x) = \begin{cases} U^i(R,\theta;\rho,\phi) = \ln R - \sum\limits_{m=1}^{\infty} \frac{1}{m}\left(\frac{\rho}{R}\right)^m \cos m(\theta-\phi), & R \geqslant \rho, \\ U^e(R,\theta;\rho,\phi) = \ln \rho - \sum\limits_{m=1}^{\infty} \frac{1}{m}\left(\frac{R}{\rho}\right)^m \cos m(\theta-\phi), & \rho > R, \end{cases} \tag{13}$$

where the superscripts "i" and "e" denote the interior ($R > \rho$) and exterior ($\rho > R$) cases, respectively. The origin of the observer system for the degenerate kernel is $(0,0)$. By setting the origin at o for the observer system, a circle with radius R from the origin o to the source point s is plotted. If the field point x is situated inside the circular region, the degenerate kernel belongs to the interior expression of U^i; otherwise, it is the exterior case. After taking the normal derivative $\partial/\partial R$ with respect to Eq. (13), the $T(s,x)$ kernel yields

$$T(s,x) = \begin{cases} T^i(R,\theta;\rho,\phi) = \frac{1}{R} + \sum\limits_{m=1}^{\infty} \left(\frac{\rho^m}{R^{m+1}}\right) \cos m(\theta-\phi), & R > \rho, \\ T^e(R,\theta;\rho,\phi) = -\sum\limits_{m=1}^{\infty} \left(\frac{R^{m-1}}{\rho^m}\right) \cos m(\theta-\phi), & \rho > R \end{cases} \tag{14}$$

and the higher-order kernel functions, $L(s, x)$ and $M(s, x)$, are shown below:

$$L(s, x) = \begin{cases} L^i(R, \theta; \rho, \phi) = -\sum_{m=1}^{\infty} \left(\frac{\rho^{m-1}}{R^m}\right) \cos m(\theta - \phi), & R > \rho, \\ L^e(R, \theta; \rho, \phi) = \frac{1}{\rho} + \sum_{m=1}^{\infty} \left(\frac{R^m}{\rho^{m+1}}\right) \cos m(\theta - \phi), & \rho > R, \end{cases}$$

(15)

$$M(s, x) = \begin{cases} M^i(R, \theta; \rho, \phi) = \sum_{m=1}^{\infty} \left(\frac{m\rho^{m-1}}{R^{m+1}}\right) \cos m(\theta - \phi), & R \geqslant \rho, \\ M^e(R, \theta; \rho, \phi) = \sum_{m=1}^{\infty} \left(\frac{mR^{m-1}}{\rho^{m+1}}\right) \cos m(\theta - \phi), & \rho > R. \end{cases}$$

(16)

Since the potentials resulted from $T(s, x)$ and $L(s, x)$ kernels are discontinuous across the boundary, the potentials of $T(s, x)$ and $L(s, x)$ for $R \to \rho^+$ and $R \to \rho^-$ are different. This is the reason why $R = \rho$ is not included for degenerate kernels of $T(s, x)$ and $L(s, x)$ in Eqs. (14) and (15). For problems with the kth circular boundary, we apply the Fourier series expansions to approximate the potential w and its normal derivative t on the boundary as

$$w(s_k) = a_0^k + \sum_{n=1}^{L} (a_n^k \cos n\theta_k + b_n^k \sin n\theta_k), \quad s_k \in B_k,$$

$$k = 0, 1, 2, \ldots, N,$$

(17)

$$t(s_k) = p_0^k + \sum_{n=1}^{L} (p_n^k \cos n\theta_k + q_n^k \sin n\theta_k), \quad s_k \in B_k,$$

$$k = 0, 1, 2, \ldots, N,$$

(18)

where N is the number of circular inclusions, $t(s_k) = \partial w(s_k)/\partial \mathbf{n}_s$, a_n^k, b_n^k, p_n^k and q_n^k $(n = 0, 1, 2, \ldots, L)$ are the Fourier coefficients and θ_k is the polar angle. In the real computation, only $2L + 1$ finite terms are considered where L indicates the truncated terms of Fourier series.

In the present application, both anti-plane mechanical and in-plane electrical fields are modeled by using the null-field formulation. Since the electric potential Φ also satisfies the Laplace equation, the variables w and $t(s) = \partial w(s)/\partial n_s$ in Eqs. (7), (8), (11), (12), (17) and (18) can be replaced by Φ and $\Psi(s) = \partial \Phi(s)/\partial n_s$.

3.2. Adaptive observer system [19,21]

After collocating points in the null-field integral equation, the boundary integrals through all the circular contours are required. Since the BIEs are obtained through the reciprocal theorem, it is frame indifferent due to the objectivity rule such that the observer system can be adaptively to locate the origin at the center of circle in the boundary integration. The adaptive observer system is chosen to fully employ the property of degenerate kernels and Fourier series. Figs. 3(a) and (b) show the boundary integration for the circular boundary in the adaptive observer system. Therefore, the origin of the observer
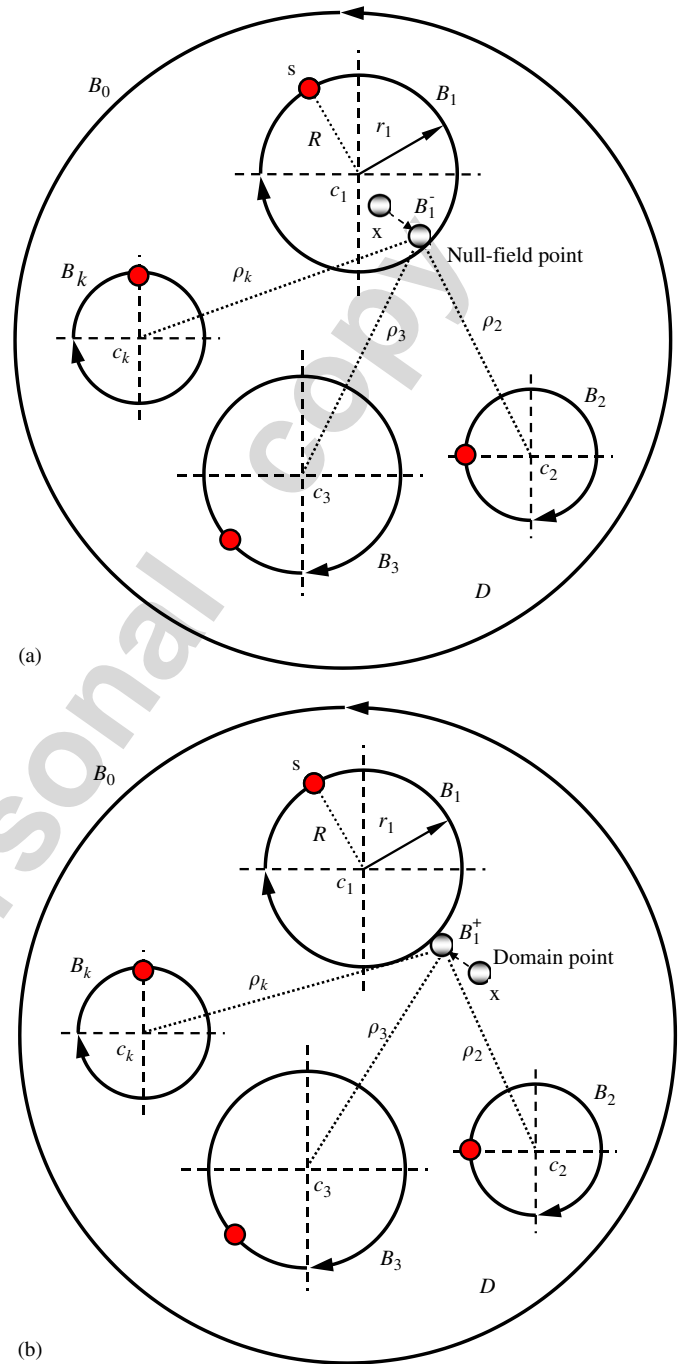

(a)

(b)

Fig. 3. (a) Sketch of the null-field integral equation for a null-field point in conjunction with the adaptive observer system ($x \notin D$, $x \to B_k$). (b) Sketch of the boundary integral equation for a domain point in conjunction with the adaptive observer system ($x \in D$, $x \to B_k$).

system is located on the center of the corresponding circle under integration to entirely utilize the geometry of circular boundary for the expansion of degenerate kernels and boundary densities. The dummy variable in the circular integration is the angle (θ) instead of the radial coordinate (R). In the present applications, the anti-plane mechanical and in-plane electrical fields can both be modeled by employing the same null-field formulation.

Table 2
Influence coefficients for the singularity distribution on the circular boundary

		$\rho < R$	$\rho > R$

$U(s, x)$

	$\rho < R$	$\rho > R$
Degenerate kernel	$U^i(R, \theta; \rho, \phi) = \ln R - \sum_{m=1}^{\infty} \frac{1}{m}\left(\frac{\rho}{R}\right)^m \cos m(\theta - \phi), \quad R \geq \rho$	$U^e(R, \theta; \rho, \phi) = \ln \rho - \sum_{m=1}^{\infty} \frac{1}{m}\left(\frac{R}{\rho}\right)^m \cos m(\theta - \phi), \quad \rho > R$
Orthogonal process	$\int_0^{2\pi} [U^i][1] R\,d\theta = 2\pi \ln R, \quad R \geq \rho$	$\int_0^{2\pi} [U^e][1] R\,d\theta = 2\pi \ln \rho, \quad \rho > R$
	$\int_0^{2\pi} [U^i][\cos n\theta] R\,d\theta = \pi \frac{1}{n} \frac{\rho^n}{R^{n-1}} \cos n\phi, \quad R \geq \rho$	$\int_0^{2\pi} [U^e][\cos n\theta] R\,d\theta = \pi \frac{1}{n} \frac{R^{n+1}}{\rho^n} \cos n\phi, \quad \rho > R$
	$\int_0^{2\pi} [U^i][\sin n\theta] R\,d\theta = \pi \frac{1}{n} \frac{\rho^n}{R^{n-1}} \sin n\phi, \quad R \geq \rho$	$\int_0^{2\pi} [U^e][\sin n\theta] R\,d\theta = \pi \frac{1}{n} \frac{R^{n+1}}{\rho^n} \sin n\phi, \quad \rho > R$
Limiting behavior across the boundary	$\lim_{\rho \to R} 2\pi \ln R = 2\pi \ln R$	$\lim_{\rho \to R} 2\pi \ln \rho = 2\pi \ln R$
	$\lim_{\rho \to R} \pi \frac{1}{n} \frac{\rho^n}{R^{n-1}} \cos n\phi = \pi \frac{1}{n} R \cos n\phi$	$\lim_{\rho \to R} \pi \frac{1}{n} \frac{R^{n+1}}{\rho^n} \cos n\phi = \pi \frac{1}{n} R \cos n\phi$
	$\lim_{\rho \to R} \pi \frac{1}{n} \frac{\rho^n}{R^{n-1}} \sin n\phi = \pi \frac{1}{n} R \sin n\phi$	$\lim_{\rho \to R} \pi \frac{1}{n} \frac{R^{n+1}}{\rho^n} \sin n\phi = \pi \frac{1}{n} R \sin n\phi$

Continuous $(R^- \to R \to R^+)$

$T(s, x)$

	$\rho < R$	$\rho > R$
Degenerate kernel	$T^i(R, \theta; \rho, \phi) = \frac{1}{R} + \sum_{m=1}^{\infty} \left(\frac{\rho^m}{R^{m+1}}\right) \cos m(\theta - \phi), \quad R > \rho$	$T^e(R, \theta; \rho, \phi) = -\sum_{m=1}^{\infty} \left(\frac{R^{m-1}}{\rho^m}\right) \cos m(\theta - \phi), \quad \rho > R$
Orthogonal process	$\int_0^{2\pi} [T^i][1] R\,d\theta = \frac{2\pi}{R}, \quad R > \rho$	$\int_0^{2\pi} [T^e][1] R\,d\theta = 0, \quad \rho > R$
	$\int_0^{2\pi} [T^i][\cos n\theta] R\,d\theta = \pi \left(\frac{\rho}{R}\right)^n \cos n\phi, \quad R > \rho$	$\int_0^{2\pi} [T^e][\cos n\theta] R\,d\theta = -\pi \left(\frac{R}{\rho}\right)^n \cos n\phi, \quad \rho > R$
	$\int_0^{2\pi} [T^i][\sin n\theta] R\,d\theta = \pi \left(\frac{\rho}{R}\right)^n \sin n\phi, \quad R > \rho$	$\int_0^{2\pi} [T^e][\sin n\theta] R\,d\theta = -\pi \left(\frac{R}{\rho}\right)^n \sin n\phi, \quad \rho > R$
Limiting behavior across the boundary	$\lim_{\rho \to R} \frac{2\pi}{R} = \frac{2\pi}{R}$	$\lim_{\rho \to R} 0 = 0$
	$\lim_{\rho \to R} \pi \left(\frac{\rho}{R}\right)^n \cos n\phi = \pi \cos n\phi$	$\lim_{\rho \to R} -\pi \left(\frac{R}{\rho}\right)^n \cos n\phi = -\pi \cos n\phi$
	$\lim_{\rho \to R} \pi \left(\frac{\rho}{R}\right)^n \sin n\phi = \pi \sin n\phi$	$\lim_{\rho \to R} -\pi \left(\frac{R}{\rho}\right)^n \sin n\phi = -\pi \sin n\phi$

Jump $(R^- \to R \to R^+)$

$L(s,x)$	Interior	Exterior
Degenerate kernel	$L^i(R,\theta;\rho,\phi) = -\sum_{m=1}^{\infty}\left(\frac{\rho^{m-1}}{R^m}\right)\cos m(\theta-\phi)$, $R>\rho$	$L^e(R,\theta;\rho,\phi) = \frac{1}{\rho} + \sum_{m=1}^{\infty}\left(\frac{R^m}{\rho^{m+1}}\right)\cos m(\theta-\phi)$, $\rho>R$
Orthogonal process	$\int_0^{2\pi}[L^i][1]Rd\theta = 0$, $R>\rho$ $\int_0^{2\pi}[L^i][\cos n\theta]Rd\theta = -\pi\left(\frac{\rho}{R}\right)^{n-1}\cos n\phi$, $R>\rho$ $\int_0^{2\pi}[L^i][\sin n\theta]Rd\theta = -\pi\left(\frac{\rho}{R}\right)^{n-1}\sin n\phi$, $R>\rho$	$\int_0^{2\pi}[L^e][1]Rd\theta = \frac{2\pi}{\rho}$, $\rho>R$ $\int_0^{2\pi}[L^e][\cos n\theta]Rd\theta = \pi\left(\frac{R}{\rho}\right)^{n+1}\cos n\phi$, $\rho>R$ $\int_0^{2\pi}[L^e][\sin n\theta]Rd\theta = \pi\left(\frac{R}{\rho}\right)^{n+1}\sin n\phi$, $\rho>R$
Limiting behavior across the boundary Jump $(R^-\to R\to R^+)$	$\lim_{\rho\to R} 0 = 0$ $\lim_{\rho\to R}-\pi\left(\frac{\rho}{R}\right)^{n-1}\cos n\phi = -\pi\cos n\phi$ $\lim_{\rho\to R}-\pi\left(\frac{\rho}{R}\right)^{n-1}\sin n\phi = -\pi\sin n\phi$	$\lim_{\rho\to R}\frac{2\pi}{\rho} = \frac{2\pi}{R}$ $\lim_{\rho\to R}\pi\left(\frac{R}{\rho}\right)^{n+1}\cos n\phi = \pi\cos n\phi$ $\lim_{\rho\to R}\pi\left(\frac{R}{\rho}\right)^{n+1}\sin n\phi = \pi\sin n\phi$

$M(s,x)$	Interior	Exterior
Degenerate kernel	$M^i(R,\theta;\rho,\phi) = \sum_{m=1}^{\infty}\left(\frac{m\rho^{m-1}}{R^{m+1}}\right)\cos m(\theta-\phi)$, $R\geq\rho$	$M^e(R,\theta;\rho,\phi) = \sum_{m=1}^{\infty}\left(\frac{mR^{m-1}}{\rho^{m+1}}\right)\cos m(\theta-\phi)$, $\rho>R$
Orthogonal process	$\int_0^{2\pi}[M^i][1]Rd\theta = 0$, $R\geq\rho$ $\int_0^{2\pi}[M^i][\cos n\theta]Rd\theta = n\pi\frac{\rho^{n-1}}{R^n}\cos n\phi$, $R\geq\rho$ $\int_0^{2\pi}[M^i][\sin n\theta]Rd\theta = n\pi\frac{\rho^{n-1}}{R^n}\sin n\phi$, $R\geq\rho$	$\int_0^{2\pi}[M^e][1]Rd\theta = 0$, $\rho>R$ $\int_0^{2\pi}[M^e][\cos n\theta]Rd\theta = n\pi\frac{R^n}{\rho^{n+1}}\cos n\phi$, $\rho>R$ $\int_0^{2\pi}[M^e][\sin n\theta]Rd\theta = n\pi\frac{R^n}{\rho^{n+1}}\sin n\phi$, $\rho>R$
Limiting behavior across the boundary Continuous $(R^-\to R\to R^+)$	$\lim_{\rho\to R} 0 = 0$ $\lim_{\rho\to R} n\pi\frac{\rho^{n-1}}{R^n}\cos n\phi = n\pi\frac{1}{R}\cos n\phi$ $\lim_{\rho\to R} n\pi\frac{\rho^{n-1}}{R^n}\sin n\phi = n\pi\frac{1}{R}\sin n\phi$	$\lim_{\rho\to R} 0 = 0$ $\lim_{\rho\to R} n\pi\frac{R^n}{\rho^{n+1}}\cos n\phi = n\pi\frac{1}{R}\cos n\phi$ $\lim_{\rho\to R} n\pi\frac{R^n}{\rho^{n+1}}\sin n\phi = n\pi\frac{1}{R}\sin n\phi$

3.3. Linear algebraic system for modeling the Laplace equation

By moving the null-field point x_m to the kth circular boundary in the limit sense for Eq. (11) in Fig. 3(a), we have

$$0 = \sum_{k=0}^{N} \int_{B_k} T(R_k, \theta_k; \rho_m, \phi_m) w(R_k, \theta_k) R_k \, d\theta_k$$
$$- \sum_{k=0}^{N} \int_{B_k} U(R_k, \theta_k; \rho_m, \phi_m) t(R_k, \theta_k) R_k \, d\theta_k,$$
$$x(\rho_m, \phi_m) \in D^c, \tag{19}$$

where N is the number of circular inclusions and B_0 denotes the outer boundary for the bounded domain. In case of the infinite problem, B_0 becomes B_∞. Note that the kernels $U(s, x)$ and $T(s, x)$ are assumed in the degenerate form given by Eqs. (13) and (14), respectively, while the boundary densities w and t are expressed in terms of the Fourier series expansion forms given by Eqs. (17) and (18), respectively. Then, the integrals multiplied by separate expansion coefficients in Eq. (19) are non-singular and the limit of the null-field point to the boundary is easily implemented by using appropriate forms of degenerate kernels. Thus, the collocation point $x(\rho_m, \phi_m)$ in the discretized Eq. (19) can be considered on the boundary B_k, as well as the null-field point. In contrast to the standard discretized BIE formulation with nodal unknowns of the physical boundary densities w and t. Now the degrees of freedom are transformed to Fourier coefficients employed in expansion of boundary densities. It is found that the compatible relationship of the boundary unknowns is equivalent by moving either the null-field point or the domain point to the boundary in different directions using various degenerate kernels as shown in Figs. 3(a) and (b). In the B_k integration, we set the origin of the observer system to collocate at the center c_k to fully utilize the degenerate kernels and Fourier series. By collocating the null-field point on the boundary, the linear algebraic system is obtained:

For the exterior problem of matrix, we have

$$[\mathbf{U}^M]\{\mathbf{t}^M - \mathbf{t}^\infty\} = [\mathbf{T}^M]\{\mathbf{w}^M - \mathbf{w}^\infty\}, \tag{20}$$

$$[\mathbf{U}^M]\{\mathbf{\Psi}^M - \mathbf{\Psi}^\infty\} = [\mathbf{T}^M]\{\mathbf{\Phi}^M - \mathbf{\Phi}^\infty\}. \tag{21}$$

For the interior problem of each inclusion, we have

$$[\mathbf{U}^I]\{\mathbf{t}^I\} = [\mathbf{T}^I]\{\mathbf{w}^I\}, \tag{22}$$

$$[\mathbf{U}^I]\{\mathbf{\Psi}^I\} = [\mathbf{T}^I]\{\mathbf{\Phi}^I\}, \tag{23}$$

where the superscripts "M" and "I" denote the matrix and inclusion, respectively. $[\mathbf{U}^M]$, $[\mathbf{T}^M]$, $[\mathbf{U}^I]$ and $[\mathbf{T}^I]$ are the influence matrices with a dimension of $(N+1)(2L+1)$ by $(N+1)(2L+1)$, $\{\mathbf{w}^M\}$, $\{\mathbf{t}^M\}$, $\{\mathbf{w}^\infty\}$, $\{\mathbf{t}^\infty\}$, $\{\mathbf{\Phi}^M\}$, $\{\mathbf{\Psi}^M\}$, $\{\mathbf{\Phi}^\infty\}$, $\{\mathbf{\Psi}^\infty\}$, $\{\mathbf{w}^I\}$, $\{\mathbf{t}^I\}$, $\{\mathbf{\Phi}^I\}$ and $\{\mathbf{\Psi}^I\}$ denote the column vectors of Fourier coefficients with a dimension of

$(N+1)(2L+1)$ by 1 in which those are defined as follows:

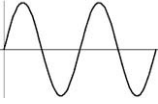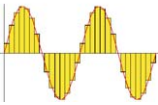$$[\mathbf{U}^M] = \begin{bmatrix} \mathbf{U}_{00}^M & \mathbf{U}_{01}^M & \cdots & \mathbf{U}_{0N}^M \\ \mathbf{U}_{10}^M & \mathbf{U}_{11}^M & \cdots & \mathbf{U}_{1N}^M \\ \vdots & \vdots & \ddots & \vdots \\ \mathbf{U}_{N0}^M & \mathbf{U}_{N1}^M & \cdots & \mathbf{U}_{NN}^M \end{bmatrix},$$

$$[\mathbf{T}^M] = \begin{bmatrix} \mathbf{T}_{00}^M & \mathbf{T}_{01}^M & \cdots & \mathbf{T}_{0N}^M \\ \mathbf{T}_{10}^M & \mathbf{T}_{11}^M & \cdots & \mathbf{T}_{1N}^M \\ \vdots & \vdots & \ddots & \vdots \\ \mathbf{T}_{N0}^M & \mathbf{T}_{N1}^M & \cdots & \mathbf{T}_{NN}^M \end{bmatrix}, \tag{24}$$

$$[\mathbf{U}^I] = \begin{bmatrix} \mathbf{U}_{00}^I & \mathbf{U}_{01}^I & \cdots & \mathbf{U}_{0N}^I \\ \mathbf{U}_{10}^I & \mathbf{U}_{11}^I & \cdots & \mathbf{U}_{1N}^I \\ \vdots & \vdots & \ddots & \vdots \\ \mathbf{U}_{N0}^I & \mathbf{U}_{N1}^I & \cdots & \mathbf{U}_{NN}^I \end{bmatrix},$$

$$[\mathbf{T}^I] = \begin{bmatrix} \mathbf{T}_{00}^I & \mathbf{T}_{01}^I & \cdots & \mathbf{T}_{0N}^I \\ \mathbf{T}_{10}^I & \mathbf{T}_{11}^I & \cdots & \mathbf{T}_{1N}^I \\ \vdots & \vdots & \ddots & \vdots \\ \mathbf{T}_{N0}^I & \mathbf{T}_{N1}^I & \cdots & \mathbf{T}_{NN}^I \end{bmatrix}, \tag{25}$$

$$\{\mathbf{w}^M\} = \begin{Bmatrix} \mathbf{w}_0^M \\ \mathbf{w}_1^M \\ \mathbf{w}_2^M \\ \vdots \\ \mathbf{w}_N^M \end{Bmatrix}, \quad \{\mathbf{t}^M\} = \begin{Bmatrix} \mathbf{t}_0^M \\ \mathbf{t}_1^M \\ \mathbf{t}_2^M \\ \vdots \\ \mathbf{t}_N^M \end{Bmatrix},$$

$$\{\mathbf{\Phi}^M\} = \begin{Bmatrix} \mathbf{\Phi}_0^M \\ \mathbf{\Phi}_1^M \\ \mathbf{\Phi}_2^M \\ \vdots \\ \mathbf{\Phi}_N^M \end{Bmatrix}, \quad \{\mathbf{\Psi}^M\} = \begin{Bmatrix} \mathbf{\Psi}_0^M \\ \mathbf{\Psi}_1^M \\ \mathbf{\Psi}_2^M \\ \vdots \\ \mathbf{\Psi}_N^M \end{Bmatrix}, \tag{26}$$

$$\{\mathbf{w}^\infty\} = \begin{Bmatrix} \mathbf{w}_0^\infty \\ \mathbf{w}_1^\infty \\ \mathbf{w}_2^\infty \\ \vdots \\ \mathbf{w}_N^\infty \end{Bmatrix}, \quad \{\mathbf{t}^\infty\} = \begin{Bmatrix} \mathbf{t}_0^\infty \\ \mathbf{t}_1^\infty \\ \mathbf{t}_2^\infty \\ \vdots \\ \mathbf{t}_N^\infty \end{Bmatrix},$$

Table 3
Comparisons of the present method and conventional BEM

	Boundary density discretization	Auxiliary system	Formulation	Observer system	Singularity	Convergence	Boundary-layer effect
Present method	Fourier series	Degenerate kernel	Null-field integral equation	Adaptive observer system	Disappear after introducing the degenerate kernel	Exponential convergence	Free
Conventional BEM	Constant element	Fundamental solution	Boundary integral equation	Fixed observer system	Principal values (C.P.V., R.P.V. and H.P.V.)	Linear algebraic convergence	Appear

where *C.P.V., R.P.V.* and *H.P.V.* are the Cauchy, Riemann and Hadamard principal values, respectively.
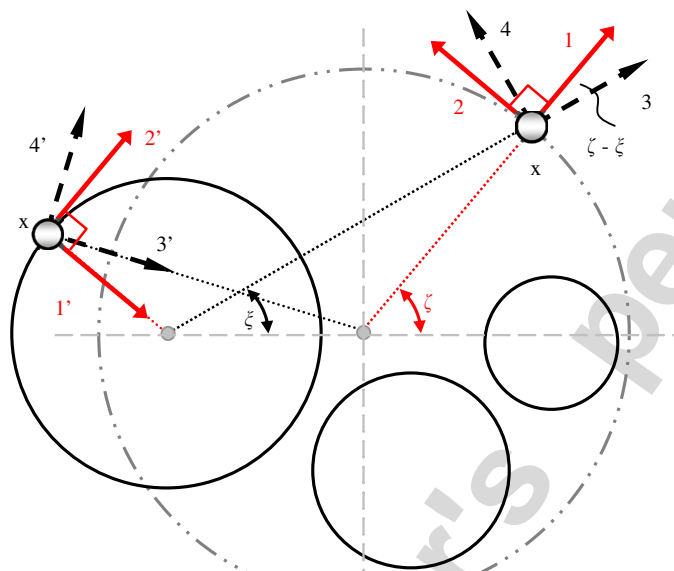

Fig. 4. Vector decomposition for the potential gradient in the hyper-singular equation. 1, 1′: Normal direction; 2, 2′: Tangential direction; 3, 3′: True normal direction; 4, 4′: True tangential direction.

$$\{\mathbf{\Phi}^{\infty}\} = \left\{ \begin{array}{c} \mathbf{\Phi}_0^{\infty} \\ \mathbf{\Phi}_1^{\infty} \\ \mathbf{\Phi}_2^{\infty} \\ \vdots \\ \mathbf{\Phi}_N^{\infty} \end{array} \right\}, \quad \{\mathbf{\Psi}^{\infty}\} = \left\{ \begin{array}{c} \mathbf{\Psi}_0^{\infty} \\ \mathbf{\Psi}_1^{\infty} \\ \mathbf{\Psi}_2^{\infty} \\ \vdots \\ \mathbf{\Psi}_N^{\infty} \end{array} \right\}, \tag{27}$$

$$\{\mathbf{w}^{\mathrm{I}}\} = \left\{ \begin{array}{c} \mathbf{w}_0^{\mathrm{I}} \\ \mathbf{w}_1^{\mathrm{I}} \\ \mathbf{w}_2^{\mathrm{I}} \\ \vdots \\ \mathbf{w}_N^{\mathrm{I}} \end{array} \right\}, \quad \{\mathbf{t}^{\mathrm{I}}\} = \left\{ \begin{array}{c} \mathbf{t}_0^{\mathrm{I}} \\ \mathbf{t}_1^{\mathrm{I}} \\ \mathbf{t}_2^{\mathrm{I}} \\ \vdots \\ \mathbf{t}_N^{\mathrm{I}} \end{array} \right\},$$

$$\{\mathbf{\Phi}^{\mathrm{I}}\} = \left\{ \begin{array}{c} \mathbf{\Phi}_0^{\mathrm{I}} \\ \mathbf{\Phi}_1^{\mathrm{I}} \\ \mathbf{\Phi}_2^{\mathrm{I}} \\ \vdots \\ \mathbf{\Phi}_N^{\mathrm{I}} \end{array} \right\}, \quad \{\mathbf{\Psi}^{\mathrm{I}}\} = \left\{ \begin{array}{c} \mathbf{\Psi}_0^{\mathrm{I}} \\ \mathbf{\Psi}_1^{\mathrm{I}} \\ \mathbf{\Psi}_2^{\mathrm{I}} \\ \vdots \\ \mathbf{\Psi}_N^{\mathrm{I}} \end{array} \right\}, \tag{28}$$

where the first subscript "j" ($j = 0, 1, 2, \ldots, N$) in $\left[\mathbf{U}_{jk}^{\mathrm{M}}\right]$, $\left[\mathbf{T}_{jk}^{\mathrm{M}}\right]$, $\left[\mathbf{U}_{jk}^{\mathrm{I}}\right]$ and $\left[\mathbf{T}_{jk}^{\mathrm{I}}\right]$ denotes the index of the jth circle where the collocation point is located and the second subscript "k" ($k = 0, 1, 2, \ldots, N$) denotes the index of the kth circle when integrating on each boundary data $\{\mathbf{w}_k^{\mathrm{M}} - \mathbf{w}_k^{\infty}\}$, $\{\mathbf{t}_k^{\mathrm{M}} - \mathbf{t}_k^{\infty}\}$, $\{\mathbf{\Phi}_k^{\mathrm{M}} - \mathbf{\Phi}_k^{\infty}\}$, $\{\mathbf{\Psi}_k^{\mathrm{M}} - \mathbf{\Psi}_k^{\infty}\}$, $\{\mathbf{w}_k^{\mathrm{I}}\}$, $\{\mathbf{t}_k^{\mathrm{I}}\}$, $\{\mathbf{\Phi}_k^{\mathrm{I}}\}$ and $\{\mathbf{\Psi}_k^{\mathrm{I}}\}$, N is the number of circular inclusions in the domain. It is noted that $\{\mathbf{w}^{\infty}\}$, $\{\mathbf{t}^{\infty}\}$, $\{\mathbf{\Phi}^{\infty}\}$ and $\{\mathbf{\Psi}^{\infty}\}$ in Fig. 2(c) are the displacement and traction fields due to the remote shear and electric loadings, respectively. The coefficient matrix of the linear algebraic system is partitioned into blocks, and each off-diagonal block corresponds to the influence matrices between two different circular boundaries. The diagonal blocks are the influence matrices due to itself in each individual circle. After uniformly collocating the point along the kth circular boundary, Eq. (19) can be calculated by employing the

relations of trigonometric function and the orthogonal property in the real computation. Only the finite L terms are used in the summation of Eqs. (17) and (18). The explicit forms of all the boundary integrals for U, T, L and M kernels are listed in Table 2. Finite values of singular integrals are easily obtained after introducing the degenerate kernel. The limiting case across the boundary ($R^- \rightarrow \rho \rightarrow R^+$) is also addressed. The continuous and jump behavior across the boundary is captured. Instead of boundary data in BEM, the Fourier coefficients become the new unknown degrees of freedom in the formulation.

Two cases may be solved in a unified manner using the null-field integral formulation:

(1) One bounded problem of circular domain in Fig. 2(b) becomes the interior problem for each inclusion.
(2) The other is unbounded, i.e., the outer boundary B_0 in Fig. 3(a) is B_∞. It is the exterior problem for the matrix as shown in Fig. 2(d).

The direction of contour integration should be determined with care, i.e., counterclockwise and clockwise

Table 4
Flowchart of the present method
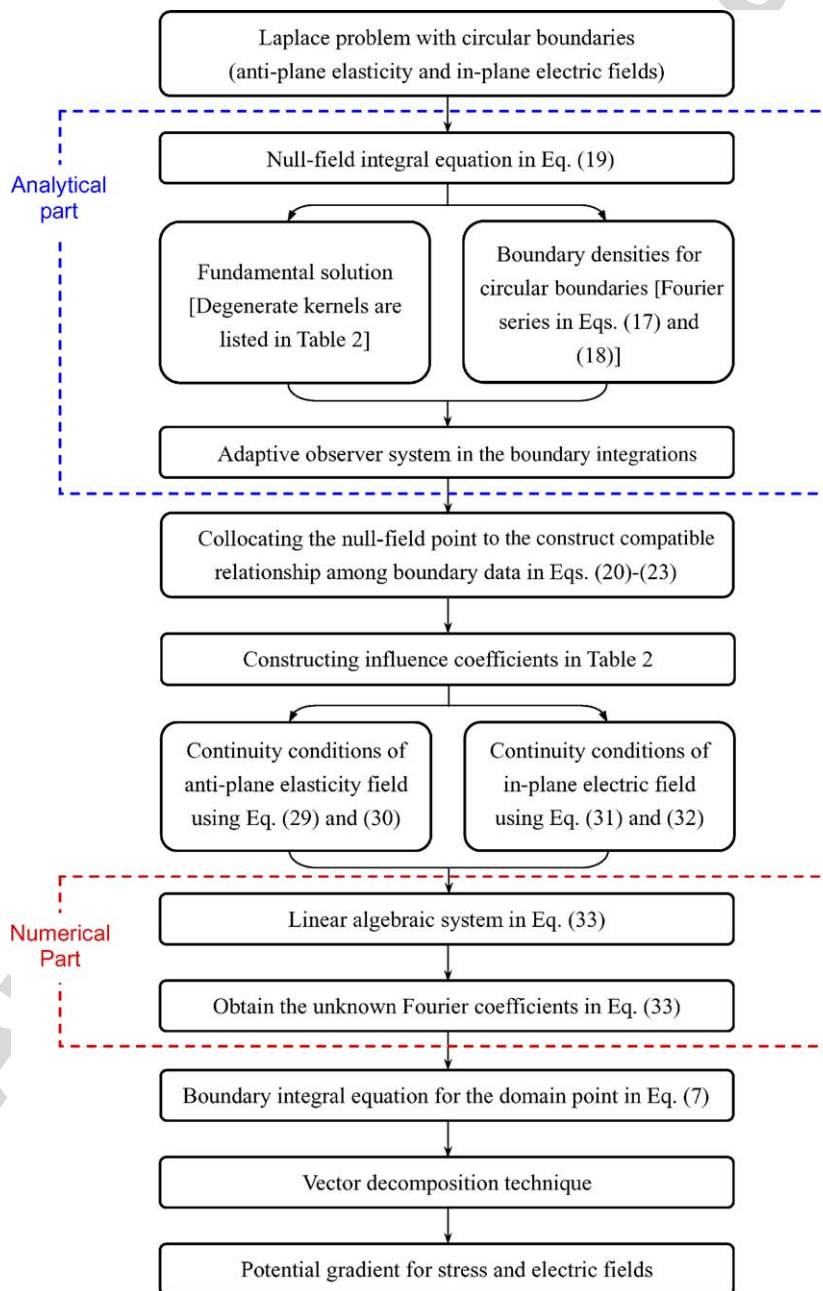
directions are used for the interior and exterior problems, respectively.

According to the continuity of displacement and equilibrium of traction along the kth interface, we have the four constraints. For the stress field, the interface condition yields

$$w^{\mathrm{M}} = w^{\mathrm{I}} \quad \text{on } B_k, \tag{29}$$

$$\sigma_{zr}^{\mathrm{M}} = \sigma_{zr}^{\mathrm{I}} \quad \text{on } B_k. \tag{30}$$

For the electric field, the interface condition yields

$$\Phi^{\mathrm{M}} = \Phi^{\mathrm{I}} \quad \text{on } B_k, \tag{31}$$

$$D_r^{\mathrm{M}} = D_r^{\mathrm{I}} \quad \text{on } B_k. \tag{32}$$

Invoking the governing equation of piezoelectricity with proper continuity conditions, fully coupled equations are obtained. By assembling the matrices in Eqs. (20)–(23) and (29)–(32), we have

$$\begin{bmatrix} \mathbf{T}^{\mathrm{M}} & -\mathbf{U}^{\mathrm{M}} & 0 & 0 & 0 & 0 & 0 & 0 \\ 0 & 0 & \mathbf{T}^{\mathrm{I}} & -\mathbf{U}^{\mathrm{I}} & 0 & 0 & 0 & 0 \\ 0 & 0 & 0 & 0 & \mathbf{T}^{\mathrm{M}} & -\mathbf{U}^{\mathrm{M}} & 0 & 0 \\ 0 & 0 & 0 & 0 & 0 & 0 & \mathbf{T}^{\mathrm{I}} & -\mathbf{U}^{\mathrm{I}} \\ \mathbf{I} & 0 & -\mathbf{I} & 0 & 0 & 0 & 0 & 0 \\ 0 & \mathbf{c}_{44}^{\mathrm{M}} & 0 & \mathbf{c}_{44}^{\mathrm{I}} & 0 & \mathbf{e}_{15}^{\mathrm{M}} & 0 & \mathbf{e}_{15}^{\mathrm{I}} \\ 0 & 0 & 0 & 0 & \mathbf{I} & 0 & -\mathbf{I} & 0 \\ 0 & \mathbf{e}_{15}^{\mathrm{M}} & 0 & \mathbf{e}_{15}^{\mathrm{I}} & 0 & -\boldsymbol{\varepsilon}_{11}^{\mathrm{M}} & 0 & -\boldsymbol{\varepsilon}_{11}^{\mathrm{I}} \end{bmatrix}$$

$$\times \begin{Bmatrix} \mathbf{w}^{\mathrm{M}} \\ \mathbf{t}^{\mathrm{M}} \\ \mathbf{w}^{\mathrm{I}} \\ \mathbf{t}^{\mathrm{I}} \\ \boldsymbol{\Phi}^{\mathrm{M}} \\ \boldsymbol{\Psi}^{\mathrm{M}} \\ \boldsymbol{\Phi}^{\mathrm{I}} \\ \boldsymbol{\Psi}^{\mathrm{I}} \end{Bmatrix} = \begin{Bmatrix} \mathbf{a} \\ 0 \\ \mathbf{b} \\ 0 \\ 0 \\ 0 \\ 0 \\ 0 \end{Bmatrix}, \tag{33}$$

where $\{\mathbf{a}\}$ and $\{\mathbf{b}\}$ are the forcing terms due to the far-field anti-plane shear and the far-field in-plane electric field as shown in Appendix, $[\mathbf{c}_{44}^{\mathrm{M}}]$, $[\mathbf{c}_{44}^{\mathrm{I}}]$, $[\mathbf{e}_{15}^{\mathrm{M}}]$, $[\mathbf{e}_{15}^{\mathrm{I}}]$, $[\boldsymbol{\varepsilon}_{11}^{\mathrm{M}}]$ and $[\boldsymbol{\varepsilon}_{11}^{\mathrm{I}}]$ are defined as follows:

$$[\mathbf{c}_{44}^{\mathrm{M}}] = \begin{bmatrix} c_{44}^{\mathrm{M}} & 0 & \cdots & 0 \\ 0 & c_{44}^{\mathrm{M}} & \cdots & 0 \\ \vdots & \vdots & \ddots & \vdots \\ 0 & 0 & \cdots & c_{44}^{\mathrm{M}} \end{bmatrix},$$

$$[\mathbf{c}_{44}^{\mathrm{I}}] = \begin{bmatrix} c_{44}^{\mathrm{I}} & 0 & \cdots & 0 \\ 0 & c_{44}^{\mathrm{I}} & \cdots & 0 \\ \vdots & \vdots & \ddots & \vdots \\ 0 & 0 & \cdots & c_{44}^{\mathrm{I}} \end{bmatrix}, \tag{34}$$

$$[\mathbf{e}_{15}^{\mathrm{M}}] = \begin{bmatrix} e_{15}^{\mathrm{M}} & 0 & \cdots & 0 \\ 0 & e_{15}^{\mathrm{M}} & \cdots & 0 \\ \vdots & \vdots & \ddots & \vdots \\ 0 & 0 & \cdots & e_{15}^{\mathrm{M}} \end{bmatrix},$$

$$[\mathbf{e}_{15}^{\mathrm{I}}] = \begin{bmatrix} e_{15}^{\mathrm{I}} & 0 & \cdots & 0 \\ 0 & e_{15}^{\mathrm{I}} & \cdots & 0 \\ \vdots & \vdots & \ddots & \vdots \\ 0 & 0 & \cdots & e_{15}^{\mathrm{I}} \end{bmatrix}, \tag{35}$$

$$[\boldsymbol{\varepsilon}_{11}^{\mathrm{M}}] = \begin{bmatrix} \varepsilon_{11}^{\mathrm{M}} & 0 & \cdots & 0 \\ 0 & \varepsilon_{11}^{\mathrm{M}} & \cdots & 0 \\ \vdots & \vdots & \ddots & \vdots \\ 0 & 0 & \cdots & \varepsilon_{11}^{\mathrm{M}} \end{bmatrix},$$

$$[\boldsymbol{\varepsilon}_{11}^{\mathrm{I}}] = \begin{bmatrix} \varepsilon_{11}^{\mathrm{I}} & 0 & \cdots & 0 \\ 0 & \varepsilon_{11}^{\mathrm{I}} & \cdots & 0 \\ \vdots & \vdots & \ddots & \vdots \\ 0 & 0 & \cdots & \varepsilon_{11}^{\mathrm{I}} \end{bmatrix}. \tag{36}$$
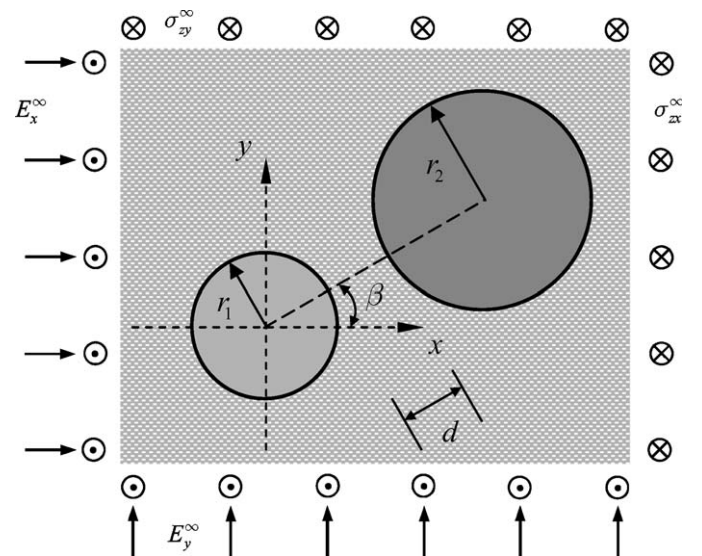

Fig. 5. Two piezoelectric circular inclusions embedded in a piezoelectric matrix under remote shear and electric loadings.
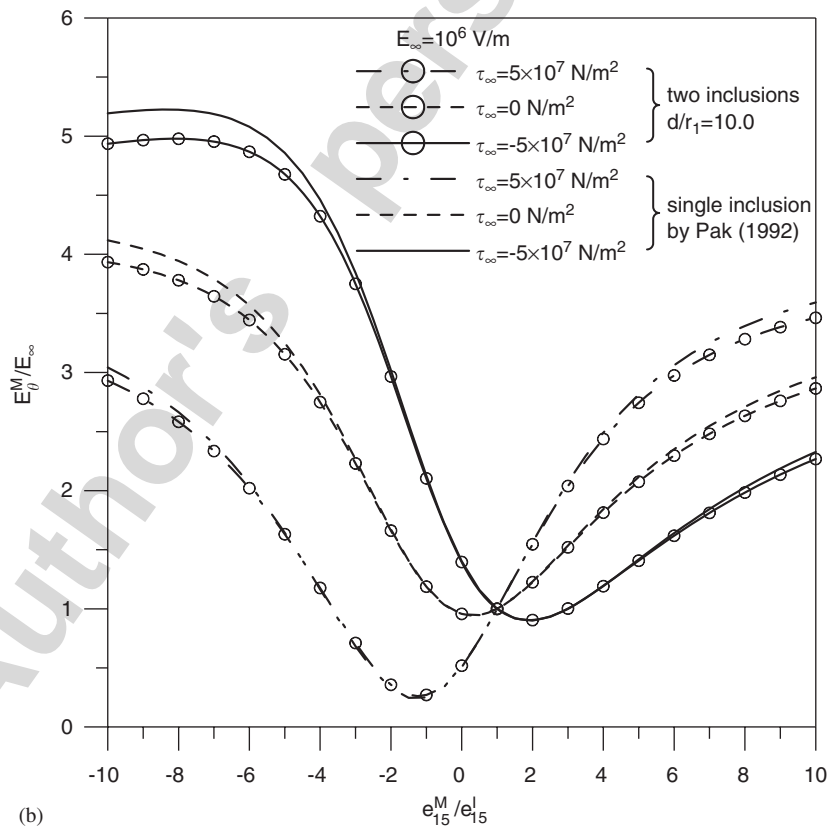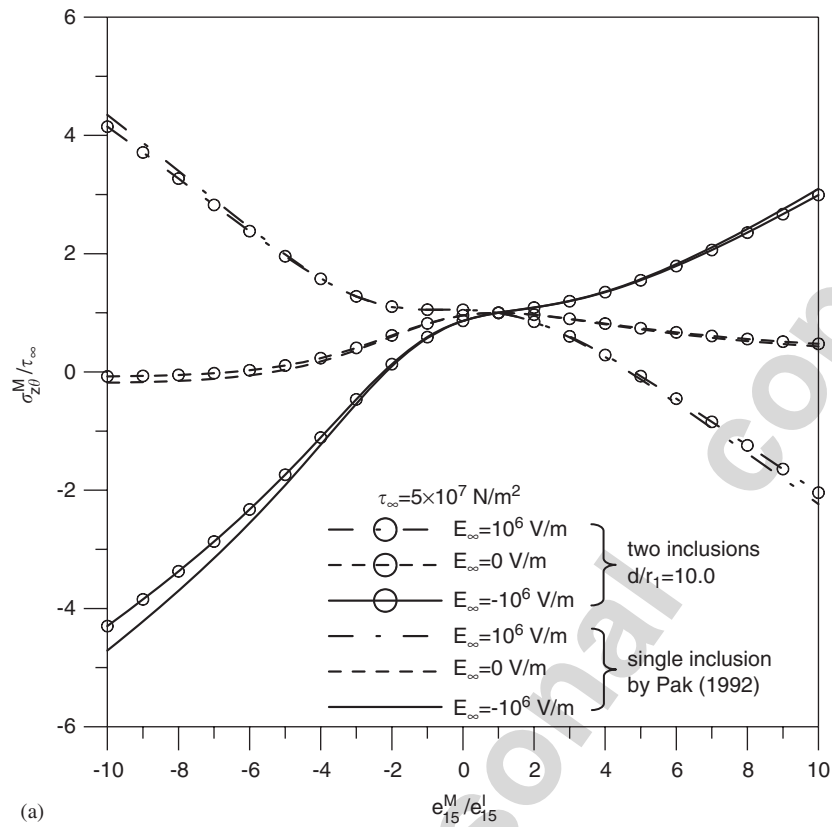
Fig. 6. (a) Stress concentration as a function of the ratio of piezoelectric constants with $\beta = 90°$. (b) Electric field concentration as a function of the ratio of piezoelectric constants with $\beta = 90°$.

The matrix $[\mathbf{I}]$ is an identity matrix. After obtaining the unknown Fourier coefficients in Eq. (33), the origin of observer system is set to c_k in the B_k integration as shown in Fig. 3(b) to obtain the field potential by employing Eq. (7). The differences between the present formulation and the conventional BEM are listed in Table 3. In determining the stress and electric field concentration, the gradient of potential should be determined with care as shown in the following section.

3.4. Vector decomposition technique for the potential gradient of w and Φ in the hypersingular equation

In order to determine the stress and electric fields, the tangential derivative should be calculated with care. Also Eq. (8) shows the normal derivative of potential for domain points. For nonconcentric cases, potential gradients should be determined with care as the source point and field point locate on different boundaries. As shown in Fig. 4, the normal direction on the boundary $(1, 1')$ should be superimposed by those of the radial derivative $(3, 3')$ and angular derivative $(4, 4')$ through the vector decomposition technique. According to the concept of vector decomposition technique, the kernel functions of Eqs. (15) and (16) can be modified to

$$L(s, x)$$

$$
= \begin{cases}
L^i(R, \theta; \rho, \phi) = -\sum_{m=1}^{\infty} \left(\frac{\rho^{m-1}}{R^m}\right) \cos m(\theta - \phi) \cos(\zeta - \xi) \\
\qquad - \sum_{m=1}^{\infty} \left(\frac{\rho^{m-1}}{R^m}\right) \sin m(\theta - \phi) \\
\qquad \times \cos\left(\frac{\pi}{2} - \zeta + \xi\right), \quad R > \rho, \\
L^e(R, \theta; \rho, \phi) = \frac{1}{\rho} + \sum_{m=1}^{\infty} \left(\frac{R^m}{\rho^{m+1}}\right) \cos m(\theta - \phi) \cos(\zeta - \xi) \\
\qquad - \sum_{m=1}^{\infty} \left(\frac{R^m}{\rho^{m+1}}\right) \sin m(\theta - \phi) \\
\qquad \times \cos\left(\frac{\pi}{2} - \zeta + \xi\right), \quad \rho > R,
\end{cases}
\tag{37}
$$

$$M(s, x)$$

$$
= \begin{cases}
M^i(R, \theta; \rho, \phi) = \sum_{m=1}^{\infty} \left(\frac{m\rho^{m-1}}{R^{m+1}}\right) \cos m(\theta - \phi) \cos(\zeta - \xi) \\
\qquad - \sum_{m=1}^{\infty} \left(\frac{m\rho^{m-1}}{R^{m+1}}\right) \sin m(\theta - \phi) \\
\qquad \times \cos\left(\frac{\pi}{2} - \zeta + \xi\right), \quad R \geqslant \rho, \\
M^e(R, \theta; \rho, \phi) = \sum_{m=1}^{\infty} \left(\frac{m R^{m-1}}{\rho^{m+1}}\right) \cos m(\theta - \phi) \cos(\zeta - \xi) \\
\qquad - \sum_{m=1}^{\infty} \left(\frac{m R^{m-1}}{\rho^{m+1}}\right) \sin m(\theta - \phi) \\
\qquad \times \cos\left(\frac{\pi}{2} - \zeta + \xi\right), \quad \rho > R,
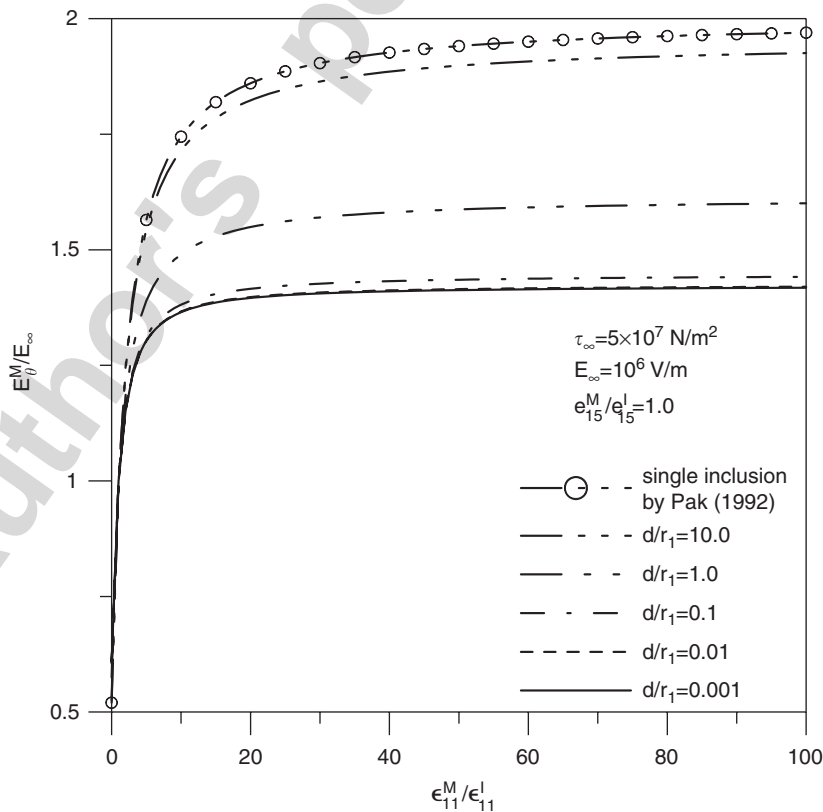\end{cases}
\tag{38}
$$

Fig. 7. Electric field concentration as a function of the ratio of dielectric constants with $e_{15}^M/e_{15}^I = 1.0$ and $\beta = 90°$.
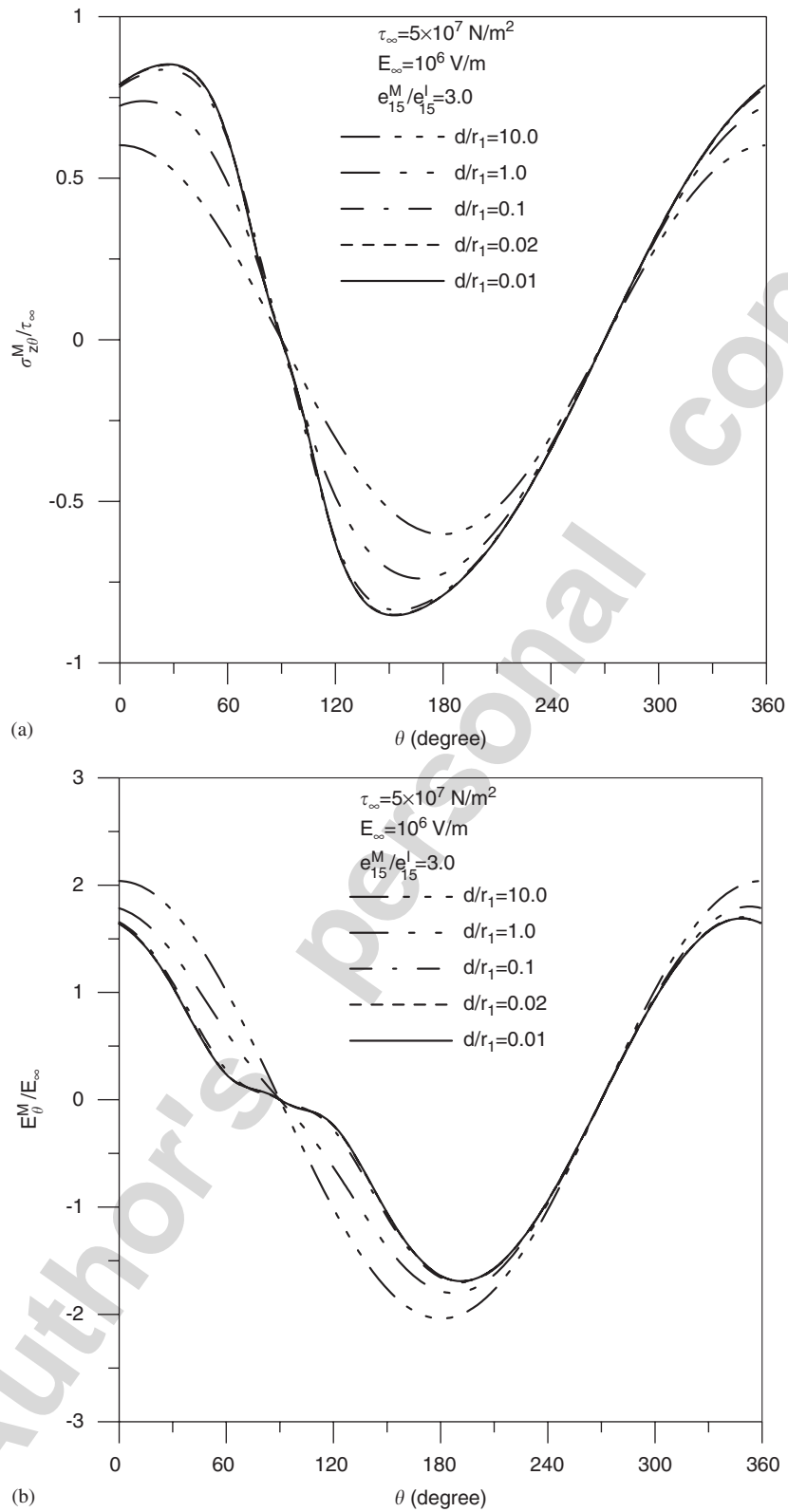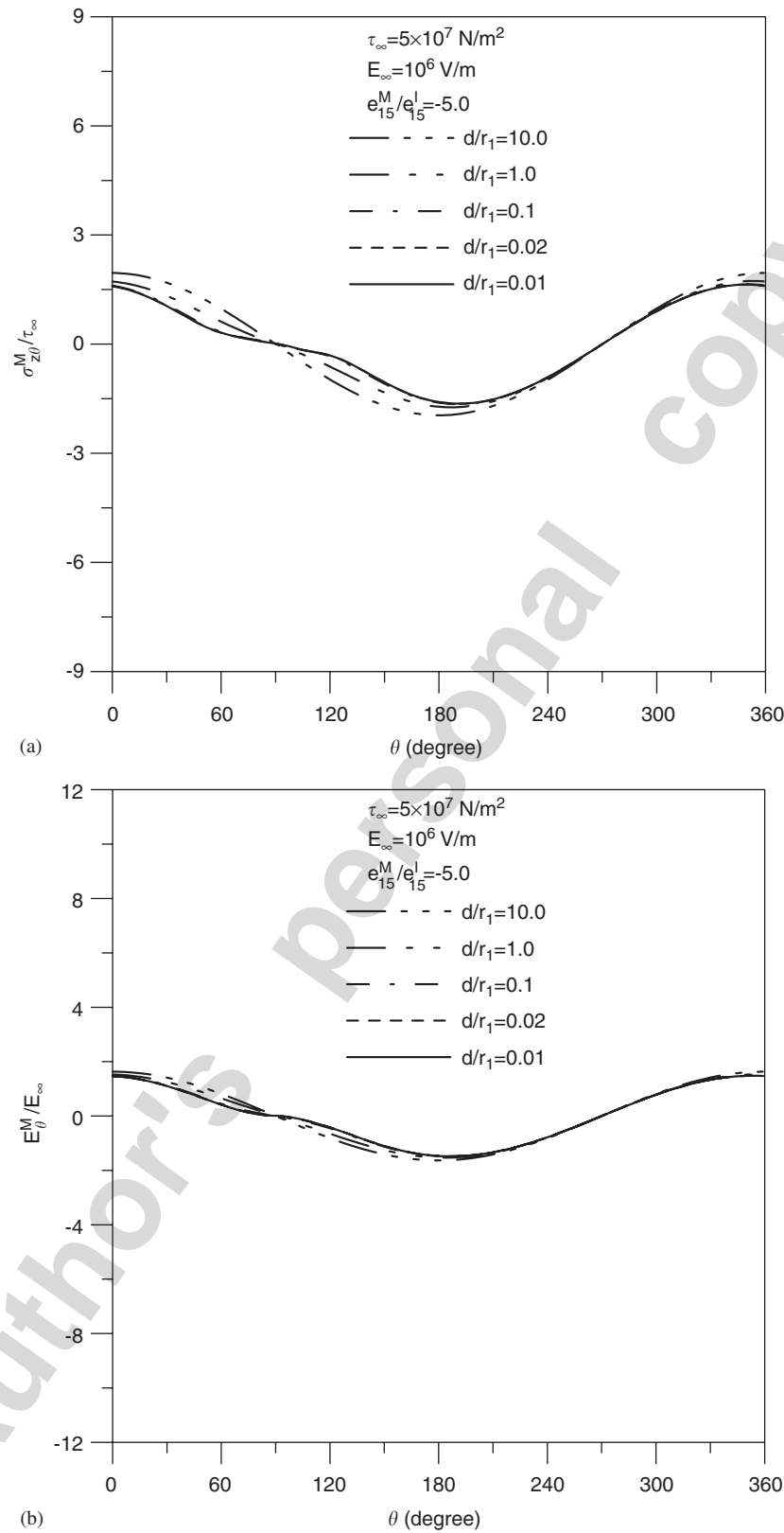
Fig. 8. (a) Tangential stress distribution for different ratios d/r_1 with $e_{15}^M/e_{15}^I = 3.0$ and $\beta = 90°$. (b) Tangential electric field distribution for different ratios d/r_1 with $e_{15}^M/e_{15}^I = 3.0$ and $\beta = 90°$.

Fig. 9. (a) Tangential stress distribution for different ratios d/r_1 with $e_{15}^M/e_{15}^I = -5.0$ and $\beta = 90°$. (b) Tangential electric field distribution for different ratios d/r_1 with $e_{15}^M/e_{15}^I = -5.0$ and $\beta = 90°$.

where ζ and ξ are shown in Fig. 4. For the confocal case, the potential gradient is derived free of special treatment since $\zeta = \xi$. The flowchart of the present method is shown in Table 4.

4. Numerical results and discussions

The exact solution for a single piezoelectric inclusion, which was derived by Pak [22], can be derived by using the present formulation. Although our formulation is general for multiple inclusions, we consider two piezoelectric circular inclusions perfectly bonded to a matrix which is subjected to the remote shear and electric field as shown in Fig. 5. In the following discussion, the applied loadings and material properties of the matrix and two inclusions are assumed as the same of Chao and Chang [24], Pak [22] and Wang and Shen [26]. All the numerical results are given below by using the 20 terms of Fourier series ($L = 20$) since those are checked to achieve good accuracy under acceptable error tolerance as compared to those by using the 30 terms.

Case 1: Two circular inclusions parallel to the applied loadings [22,24]

In order to examine the accuracy of the present formulation, the stress concentration factor $\sigma_{z\theta}/\tau_\infty$ in the matrix at $\theta = 0^\circ$ under remote loadings of $\sigma_{zx}^\infty = 0$, $\sigma_{zy}^\infty = \tau_\infty$ and $E_x^\infty = 0$, $E_y^\infty = E_\infty$ is plotted in Fig. 6(a) as a function of the ratio of piezoelectric constants e_{15}^M/e_{15}^I, where the two circular inclusions ($r_2 = 2r_1$) are arrayed parallel to the applied loadings ($\beta = 90^\circ$) and the distance between two circular inclusions $d/r_1 = 10$. It is found that the results displayed in Fig. 6(a) agree very well with the Chao and Chang's results [24] and approach to the Pak's solution of a single inclusion [22]. The electric field concentration E_θ/E_∞ in the matrix at $\theta = 0^\circ$ is plotted in Fig. 6(b) as a function of the ratio of piezoelectric constants. It is also found that the results in Fig. 6(b) leads to the Pak's solution of a single inclusion [22], since the two inclusions displace far away ($d/r_1 = 10$). The electric field concentration E_θ/E_∞ occurring at $\theta = 0^\circ$ is plotted in Fig. 7 as a function of the ratio of dielectric constants $\varepsilon_{11}^M/\varepsilon_{11}^I$. It is shown that the electric field concentration approaches two for a large value of $\varepsilon_{11}^M/\varepsilon_{11}^I$ as $d/r_1 = 10$ which is consistent with the Chao and Chang's results [24] and reduces to the Pak's solution of a single inclusion [22]. When the two inclusions approach each other, both the tangential stress $\sigma_{z\theta}$ and tangential electric field E_θ in the matrix along the boundary of the smaller inclusion are plotted in Figs. 8(a) and (b), respectively, as the piezoelectric constants are fixed at $e_{15}^M/e_{15}^I = 3$. Figs. 9(a) and (b), respectively, show the tangential stress and tangential electric field distribution that the matrix is subjected to the reversal of the poling direction as compared to the inclusion such as the ratio of piezoelectric constants $e_{15}^M/e_{15}^I = -5$. The two figures show the consistency between the present data and those of Chao and Chang in the range of $\theta = 0^\circ$–180° except near $\theta = 90^\circ$. It is
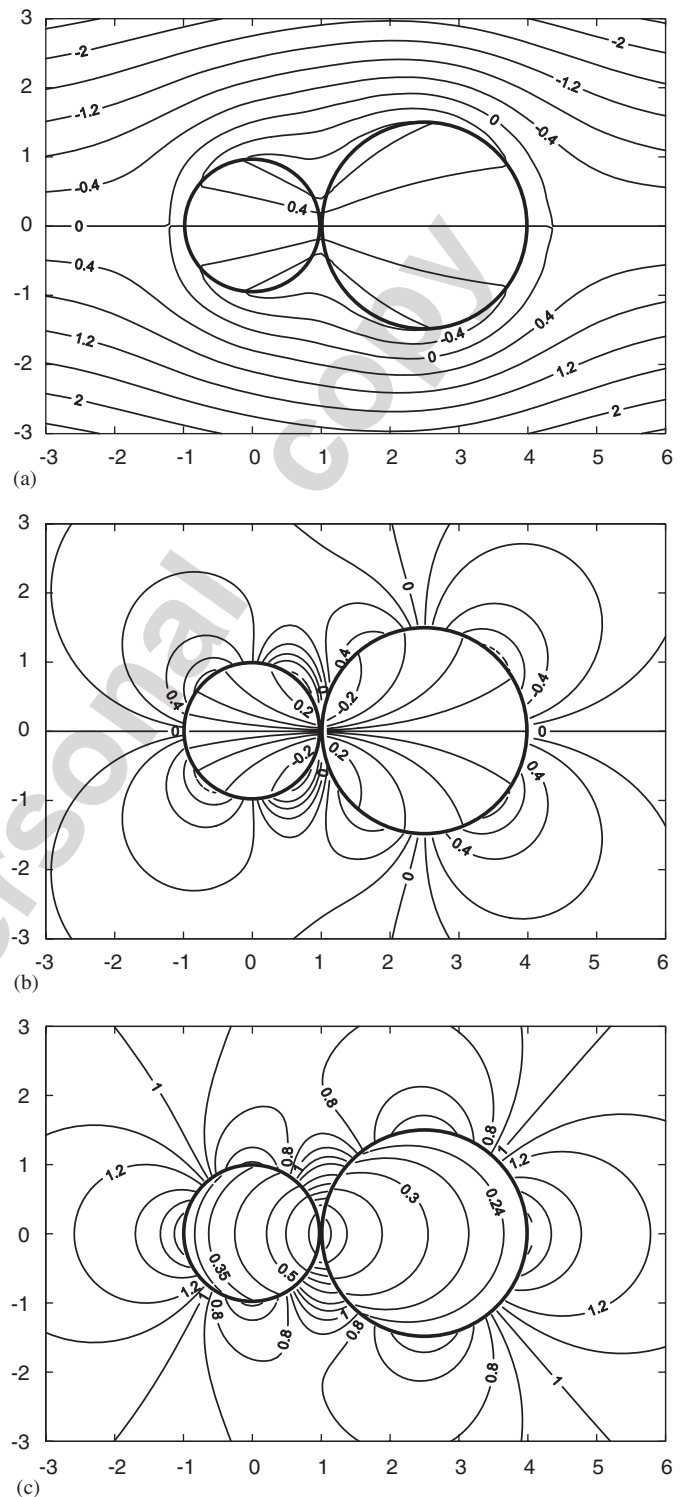

Fig. 10. (a) Contour of electric potential Φ/E_∞ ($\beta = 0^\circ$). (b) Contour of shear stress σ_{zx}/τ_∞ ($\beta = 0^\circ$). (c) Contour of shear stress σ_{zy}/τ_∞ ($\beta = 0^\circ$).

open for discussions why our results are different from those of Chao and Chang near $\theta = 90^\circ$. The tangential stress and tangential electric field are continuous across $\theta = 90^\circ$ using our formulation while the results of Chao
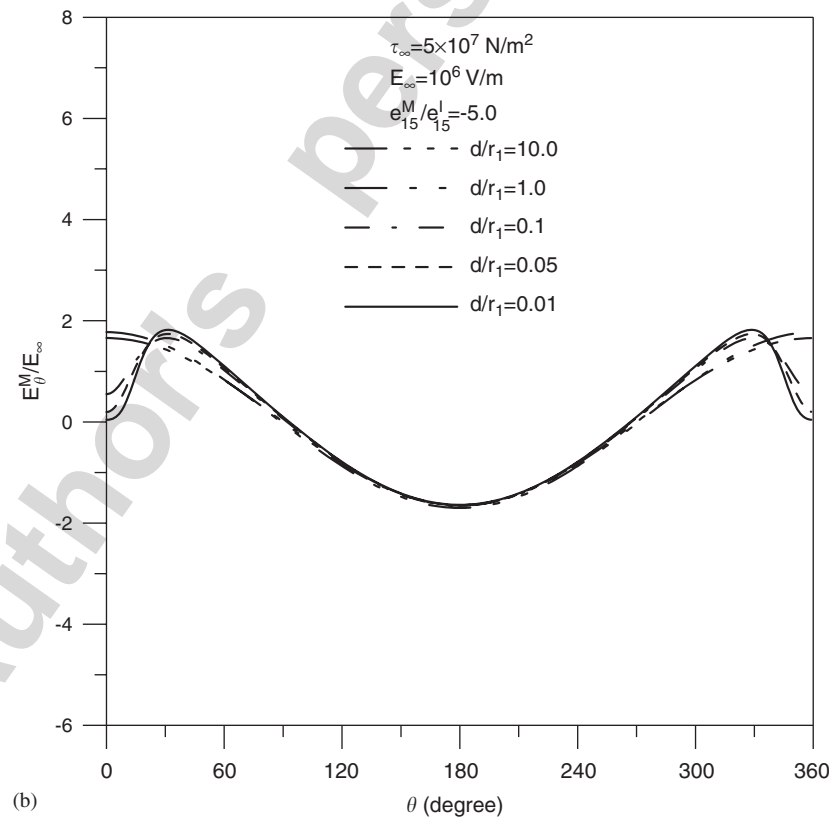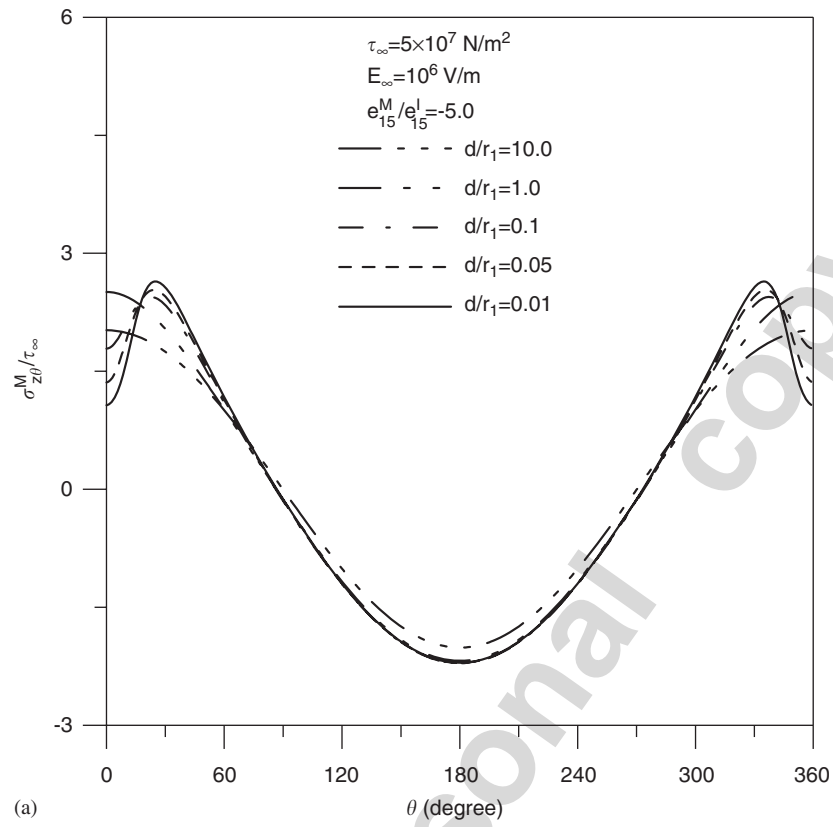
Fig. 11. (a) Tangential stress distribution for different ratios d/r_1 with $e_{15}^M/e_{15}^I = -5.0$ and $\beta = 0°$. (b) Tangential electric field distribution for different ratios d/r_1 with $e_{15}^M/e_{15}^I = -5.0$ and $\beta = 0°$.
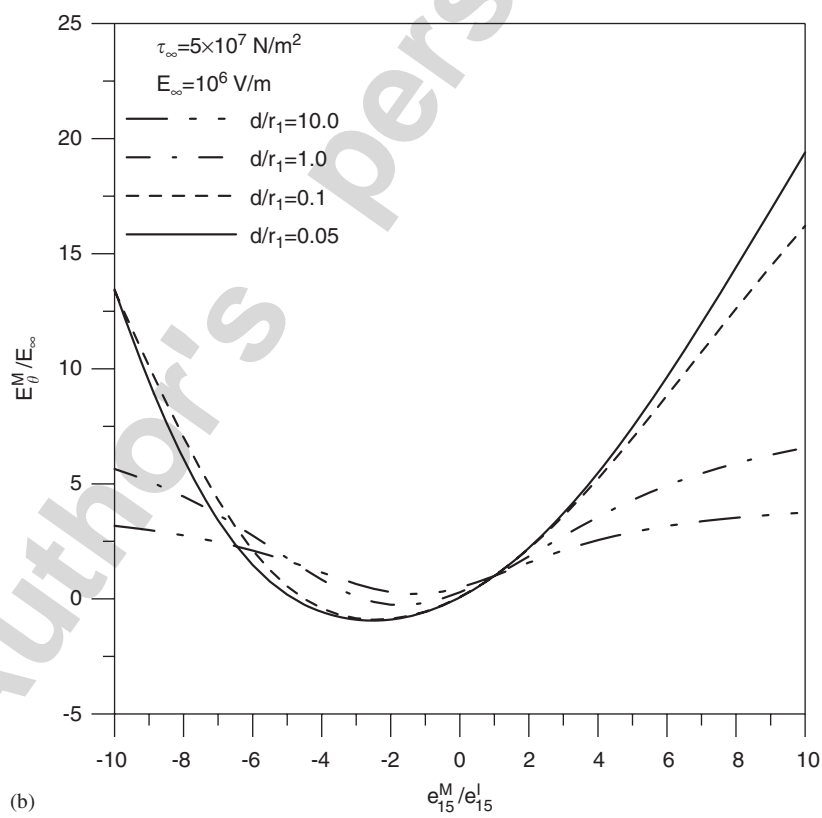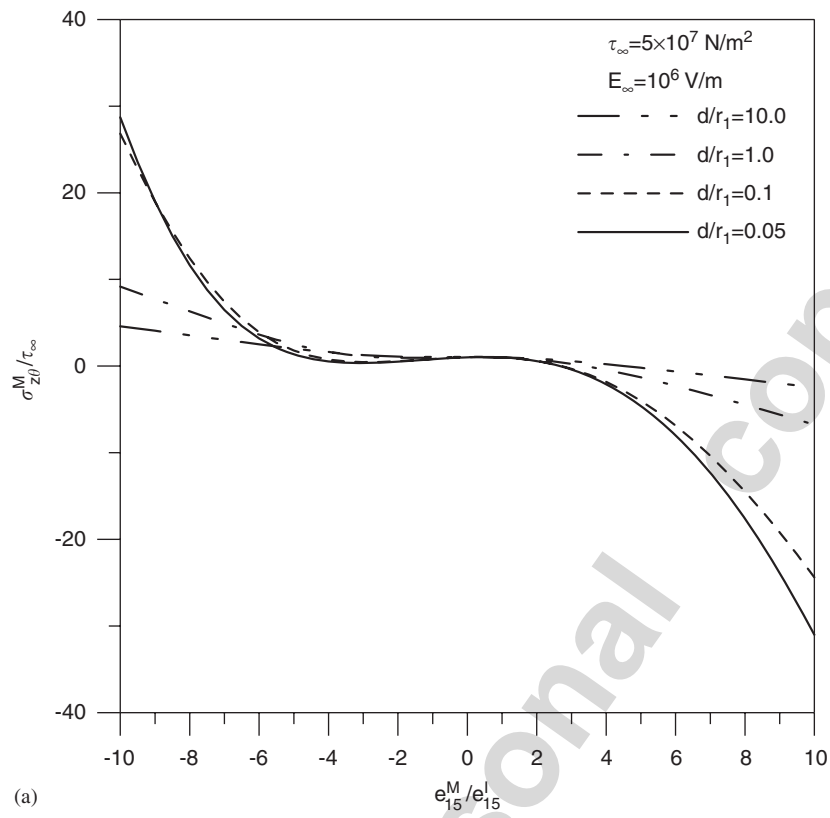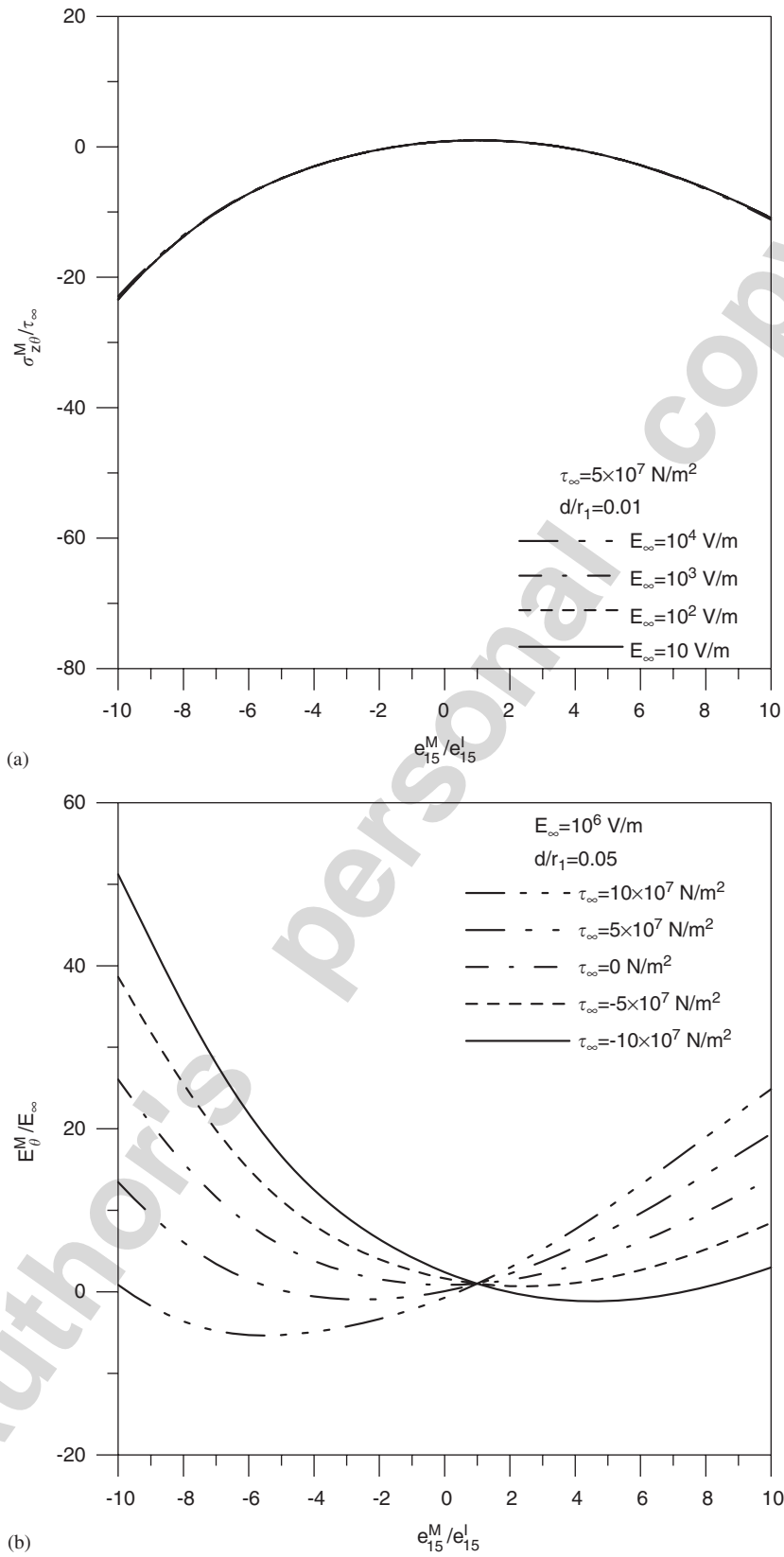
Fig. 12. (a) Stress concentration as a function of the ratio of piezoelectric constants with $\beta = 0°$. (b) Electric field concentration as a function of the ratio of piezoelectric constants with $\beta = 0°$.

Fig. 13. (a) Stress concentration as a function of the ratio of piezoelectric constants with $\beta = 0°$. (b) Electric field concentration as a function of the ratio of piezoelectric constants with $\beta = 0°$.

and Chang seems to have a jump at $\theta = 90°$ for the case of $d/r_1 = 0.01, 0.02$.

Case 2: Two circular inclusions perpendicular to the applied loadings [24,26]

As the two circular inclusions are arrayed perpendicular to the applied loadings ($\beta = 0°$), the contours of electric potential and shear stress are plotted in Figs. 10(a)–(c). The contours of shear stress match very well with the Wang and Shen's results [26]. It reveals that Φ and σ_{zx} are antisymmetric with respect to the *x*-axis and σ_{zy} is symmetric with respect to the *x*-axis. There exists serious amplification at the point where the two inclusions are nearly in contact with each other. The electric potential is continuous across the interface between the matrix and each inclusion. When the two inclusions approach each other, both the tangential stress $\sigma_{z\theta}$ and tangential electric field E_θ in the matrix along the boundary of the smaller inclusion are plotted in Figs. 11(a) and (b), respectively, as the piezoelectric constants are fixed at $e_{15}^M/e_{15}^I = -5$. After comparing with the results of Chao and Chang [24], agreement is made except near $\theta = 0°$ and $180°$. Variations of stress and electric field concentrations occurred at $\theta = 0°$ with the ratio of piezoelectric constants are shown in Figs. 12(a) and (b). It is seen that, from Figs. 12(a)–13(b), both the stress and electric field concentrations are equal to one as

$e_{15}^M/e_{15}^I = 1$ which are reasonable results for the homogeneous problem. The stress and electric field concentrations are plotted in Figs. 13(a) and (b) under loadings of various magnitude for a far-field in-plane electric load $E_y^\infty = E_\infty$ and a far-field anti-plane shear $\sigma_{zy}^\infty = \tau_\infty$, respectively. After comparing with the results of Chao and Chang [24], agreement is made except for the negative value of e_{15}^M/e_{15}^I. However, our results are smoother as shown in Figs. 12(a)–13(b) which are different from the oscillation behavior in the Chao and Chang's paper [24].

Case 3: Two circular inclusions under the applied loadings in two directions [26]

The radii of two circular inclusions are r_1 and r_2 with $r_2 = 1.5r_1$ and the problem is subjected to the remote shear $\sigma_{zx}^\infty = \tau_\infty/2$, $\sigma_{zy}^\infty = \tau_\infty$ and the electric field $E_x^\infty = E_\infty/2$, $E_y^\infty = E_\infty$. The distance between the two inclusions is $d = 0.01r_1$ and the orientation is $\beta = 0°$. Fig. 14 shows that the stress and electric displacement distribution along the *x*-axis. It can be observed that σ_{zx} and D_x are continuous while σ_{zy} and D_y are discontinuous across the interface between the matrix and inclusions. We also note that the stress and electric displacement are not uniform within the two inclusions. Fig. 15 shows the stress and electric displacement distribution along the interface between the matrix and the smaller inclusion. Fig. 16 shows the stress and electric
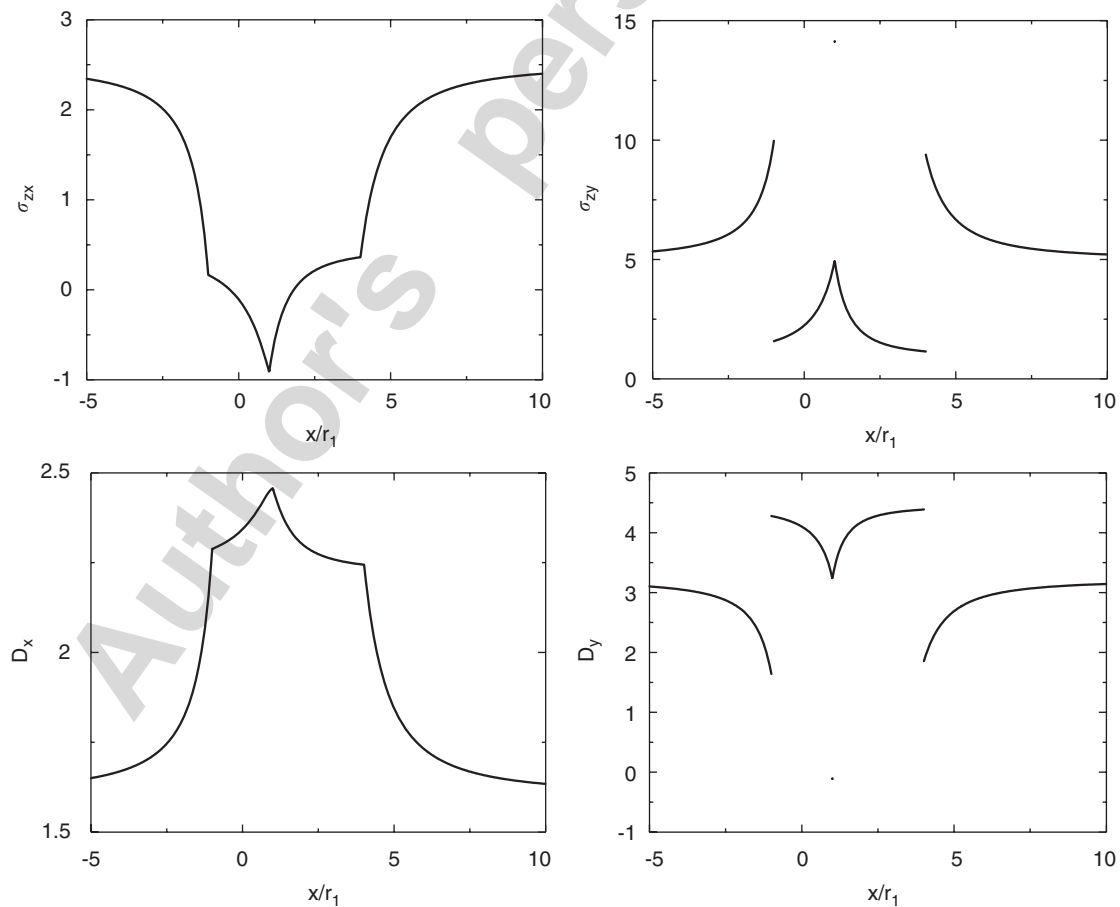

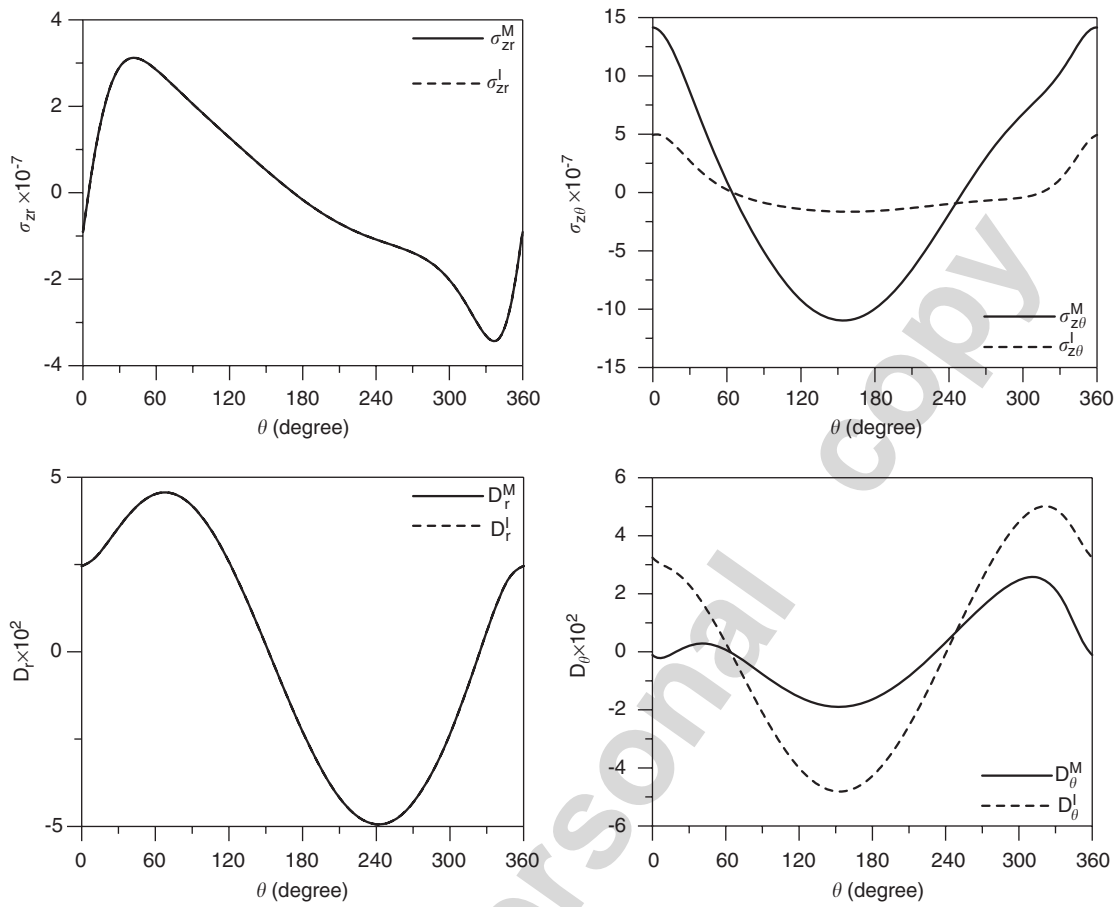Fig. 14. Stress and electric displacement distributions along the *x*-axis.

Fig. 15. Stress and electric displacement distributions along the interface between the matrix and the smaller inclusion.

displacement distribution along the interface between the matrix and the larger inclusion. According to these curves, it is found that the normal stress σ_{zr} and electric displacement D_r in the matrix and inclusion are continuous through the interface due to the continuity requirement. The present results agree very well with the Wang and Shen's results [26].

It is noted that only a fewer inclusions are considered in the demonstrate examples. For large-scale problems (e.g., more than 20 inclusions), fast algorithm [13] is required on the limitation of PC hardware. This is our future study.

5. Conclusions

The present work not only demonstrated an elegant method for solving boundary value problems but also understood the interesting coupling behaviors between mechanical and electrical fields that have not been studied previously by using BIE. It was shown that the concentration behavior of stress and electric fields depends on the distance between two piezoelectric inclusions, the mismatch in the material constants and the magnitude of mechanical and electromechanical loadings. Singularity free and boundary-layer effect free are the main gains using the present formulation as well as the exponential convergence. The present study is useful in designing piezoelectric composites and in understanding the coupling effects of two inclusions.

Appendix. Calculation for the forcing term

According to the constitutive equation due to the coupling behavior in Eq. (4), the displacement and traction fields in the infinite medium due to the far-field shear σ_{zx}^{∞}, σ_{zy}^{∞} and electric field E_x^{∞}, E_y^{∞} in Fig. 2(c) yield

$$w^{\infty} = \frac{\sigma_{zx}^{\infty} + e_{15}^{M} E_x^{\infty}}{c_{44}^{M}} x + \frac{\sigma_{zy}^{\infty} + e_{15}^{M} E_y^{\infty}}{c_{44}^{M}} y, \qquad \text{(A.1)}$$

$$t^{\infty} = \frac{\partial w^{\infty}}{\partial n} = -\left(\frac{\sigma_{zx}^{\infty} + e_{15}^{M} E_x^{\infty}}{c_{44}^{M}} n_x + \frac{\sigma_{zy}^{\infty} + e_{15}^{M} E_y^{\infty}}{c_{44}^{M}} n_y \right), \qquad \text{(A.2)}$$

where the unit outward normal vector on the boundary is $n = (n_x, n_y)$. By comparing Eq. (20) with the first row
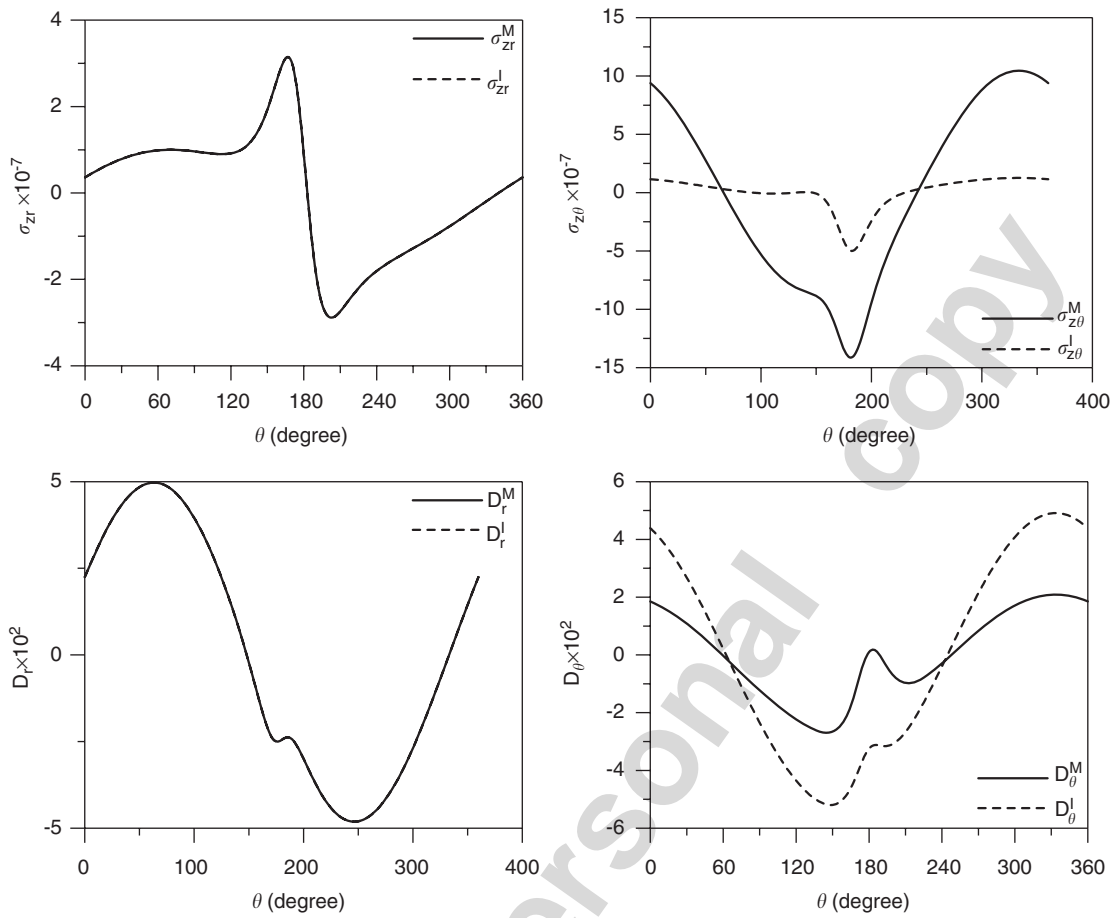
Fig. 16. Stress and electric displacement distributions along the interface between the matrix and the larger inclusion.

of Eq. (33), we have

$$\{\mathbf{a}\} = [\mathbf{T}^{\mathrm{M}}]\{\mathbf{w}^\infty\} - [\mathbf{U}^{\mathrm{M}}]\{\mathbf{t}^\infty\}. \tag{A.3}$$

For the circular boundary which the original system is located, the boundary conditions due to the far-field shear and electric field are

$$w_1^\infty = \frac{\sigma_{zx}^\infty + e_{15}^{\mathrm{M}} E_x^\infty}{c_{44}^{\mathrm{M}}} r_1 \cos \theta_1 + \frac{\sigma_{zy}^\infty + e_{15}^{\mathrm{M}} E_y^\infty}{c_{44}^{\mathrm{M}}} r_1 \sin \theta_1, \tag{A.4}$$

$$t_1^\infty = -\left(\frac{\sigma_{zx}^\infty + e_{15}^{\mathrm{M}} E_x^\infty}{c_{44}^{\mathrm{M}}} \cos \theta_1 + \frac{\sigma_{zy}^\infty + e_{15}^{\mathrm{M}} E_y^\infty}{c_{44}^{\mathrm{M}}} \sin \theta_1 \right). \tag{A.5}$$

Considering the boundary condition, due to the far-field shear and electric field, on the kth circular boundary with respect to the observer system, we have

$$w_k^\infty = \frac{\sigma_{zx}^\infty + e_{15}^{\mathrm{M}} E_x^\infty}{c_{44}^{M}} (e_x + r_k \cos \theta_k)$$
$$+ \frac{\sigma_{zy}^\infty + e_{15}^{\mathrm{M}} E_y^\infty}{c_{44}^{\mathrm{M}}} (e_y + r_k \sin \theta_k), \tag{A.6}$$

$$t_k^\infty = \left(\frac{\sigma_{zx}^\infty + e_{15}^{\mathrm{M}} E_x^\infty}{c_{44}^{\mathrm{M}}} \cos \theta_k + \frac{\sigma_{zy}^\infty + e_{15}^{\mathrm{M}} E_y^\infty}{c_{44}^{\mathrm{M}}} \sin \theta_k \right), \tag{A.7}$$

where e_x and e_y, respectively, denote the eccentric distance of kth inclusion in the x and y direction. By comparing Eq. (A.5) with (A.7), we find that t^∞ can be described in any observer system without any change, where θ_k denotes the polar angle in the adaptive observer coordinate system. For the forcing term $\{\mathbf{b}\}$ due to the far-field electric field without the coupling behavior, it can be obtained in a similar way as the forcing term $\{\mathbf{a}\}$.

References

[1] Honein E, Honein T, Herrmann G. On two circular inclusions in harmonic problems. Q Appl Math 1992;50:479–99.
[2] Steif PS. Shear stress concentration between holes. ASME J Appl Mech 1989;56:719–21.
[3] Budiansky B, Carrier GF. High shear stresses in stiff-fiber composites. ASME J Appl Mech 1984;51:733–5.
[4] Zimmerman RW. Second-order approximation for the compression of an elastic plate containing a pair of circular holes. Z Angew Math Mech 1988;68:575–7.
[5] Sendeckyj GP. Multiple circular inclusion problems in longitudinal shear deformation. J Elasticity 1971;1:83–6.

[6] Goree JG, Wilson HB. Transverse shear loading in an elastic matrix containing two circular cylindrical inclusions. ASME J Appl Mech 1967;34:511–3.

[7] Bird MD, Steele CR. A solution procedure for Laplace's equation on multiply-connected circular domains. ASME J Appl Mech 1992;59: 398–404.

[8] Chao CK, Young CW. On the general treatment of multiple inclusions in antiplane elastostatics. Int J Solids Struct 1998;35: 3573–93.

[9] Gong SX. Antiplane interaction among multiple circular inclusions. Mech Res Commun 1995;22:257–62.

[10] Ang WT, Kang I. A complex variable boundary element method for elliptic partial differential equations in a multiple-connected region. Int J Comput Math 2000;75:515–25.

[11] Chou SI. Stress field around holes in antiplane shear using complex variable boundary element method. ASME J Appl Mech 1997;64: 432–5.

[12] Mogilevskaya SG, Crouch SL. A Galerkin boundary integral method for multiple circular elastic inclusions. Int J Numer Methods Eng 2001;52:1069–106.

[13] Wang J, Crouch SL, Mogilevskaya SG. A fast and accurate algorithm for a Galerkin boundary integral method. Comput Mech 2005;37:96–109.

[14] Chen JT, Wu CS. Alternative derivations for the Poisson integral formula. Int J Math Educ Sci Technol 2006;37:165–85.

[15] Kress R. Linear integral equations. Berlin: Springer; 1989.

[16] Chen JT, Kuo SR, Chen KH. A nonsingular integral formulation for the Helmholtz eigenproblems of a circular domain. J Chin Inst Eng 1999;22:729–39.

[17] Chen JT, Kuo SR. On fictitious frequencies using circulants for radiation problems of a cylinder. Mech Res Commun 2000;27:49–58.

[18] Chen JT, Kuo SR, Lin JH. Analytical study and numerical experiments for degenerate scale problems in the boundary element

[19] Chen JT, Shen WC, Wu AC. Null-field integral equations for stress field around circular holes under antiplane shear. Eng Anal Bound Elem 2006;30:205–17.

[20] Chen JT, Shen WC, Chen PY. Analysis of circular torsion bar with circular holes using null-field approach. Comput Model Eng Sci 2006;12(2):109–19.

[21] Chen JT, Hsiao CC, Leu SY. Null-field integral equation approach for plate problems with circular boundaries. ASME J Appl Mech 2006;73:619–93.

[22] Pak YE. Circular inclusion problem in antiplane piezoelectricity. Int J Solids Struct 1992;29:2403–19.

[23] Honein T, Honein BV, Honein E, Herrmann G. On the interaction of two piezoelectric fibers embedded in an intelligent material. J Intell Mater Syst Struct 1995;6:229–36.

[24] Chao CK, Chang KJ. Interacting circular inclusions in antiplane piezoelectricity. Int J Solids Struct 1999;36:3349–73.

[25] Wu LZ, Funami K. The electro-elastic field of the infinite piezoelectric medium with two piezoelectric circular cylindrical inclusions. Acta Mech Sinica 2002;18:368–85.

[26] Wang X, Shen YP. On double circular inclusion problem in antiplane piezoelectricity. Int J Solids Struct 2001;38:4439–61.

[27] Bleustein JL. New surface wave in piezoelectric materials. Appl Phys Lett 1968;13:412–3.

[28] Emets YP, Onofrichuk YP. Interaction forces of dielectric cylinders in electric fields. IEEE Trans Dielectr Electr Insul 1996;3(1):87–98.

[29] Chen JT, Hong H-K. Review of dual boundary element methods with emphasis on hypersingular integrals and divergent series. ASME Appl Mech Rev 1999;52:17–33.

[30] Chen JT, Chiu YP. On the pseudo-differential operators in the dual boundary integral equations using degenerate kernels and circulants. Eng Anal Bound Elem 2002;26:41–53.